



Linkages between ocean circulation and the Northeast Greenland Ice Stream in the Early Holocene



Joanna Davies^{a,*}, Anders Møller Mathiasen^a, Kristiane Kristiansen^a,
Katrine Elnegaard Hansen^a, Lukas Wacker^b, Aage Kristian Olsen Alstrup^c,
Ole Lajord Munk^c, Christof Pearce^a, Marit-Solveig Seidenkrantz^a

^a Department of Geoscience, Arctic Research Centre and iClimate, Aarhus University, Aarhus, Denmark

^b Laboratory of Ion Beam Physics, ETH Zürich, Zürich, Switzerland

^c Department of Nuclear Medicine & PET, Aarhus University Hospital and Department of Clinical Medicine, Aarhus University, Aarhus, Denmark

ARTICLE INFO

Article history:

Received 24 February 2022

Received in revised form

20 April 2022

Accepted 20 April 2022

Available online xxx

Handling Editor: Dr A. Voelker

Keywords:

Holocene

Paleoceanography

Greenland

Micropaleontology

Foraminifera

Sedimentology-marine cores

ABSTRACT

The melting of marine terminating glaciers in Northeast Greenland is a visible sign that our climate is changing. This melt has been partly attributed to changes in oceanic heat fluxes, particularly warming of Atlantic Water (AW). Yet our understanding of the interaction between glaciers and the ocean is limited by the length of instrumental records. Here, we present a multi-proxy study (benthic foraminifera assemblages, CT scans, grain size, XRF, and stable isotope data) on core DA17-NG-ST08-092G, located 90 km east of the Northeast Greenland Ice Stream (NEGIS). Whilst the exact timing of deglaciation is uncertain, it is certain to have occurred at least as early as 12.5 ka cal BP, and likely before 13.4 ka cal BP. The inflow of AW may have played a role in the seemingly early deglaciation on the Northeast Greenland continental shelf. Following deglaciation, the site was overlain by an ice shelf, with AW and Polar Water (PW) flowing beneath until 11.2 ka cal BP. The NEGIS briefly retreated westwards between 11.2 and 10.8 ka cal BP before our site returned to glacier-proximal conditions dominated by colder subsurface water and persistent AW flowing beneath (10.8–9.6 ka cal BP). Between 9.6 and 7.9 ka cal BP the NEGIS retreated westwards; there was a continued presence of AW and PW at the site. A drastic shift in ocean circulation occurred at 7.9 ka cal BP, with a decline in AW flow and dominance of PW flowing beneath perennial sea ice. During the Late Holocene, there was return of AW and likely breakup of perennial sea ice.

© 2022 The Authors. Published by Elsevier Ltd. This is an open access article under the CC BY license (<http://creativecommons.org/licenses/by/4.0/>).

1. Introduction

Climate change has affected the Arctic dramatically in recent decades: mass loss from the Greenland Ice Sheet has accelerated (Enderlin et al., 2014; Shepherd et al., 2020) and Arctic sea ice has retreated and thinned (Stroeve et al., 2012). Around 60% of the increased mass loss from the Greenland Ice Sheet (1991–2015) can be attributed to changes in the surface mass balance; the remainder stems from solid ice discharge across the grounding line (van den Broeke et al., 2016). It is suggested that oceanic heat fluxes have been the dominant driver of marine terminating glacier speedup and retreat (Holland et al., 2008; Nick et al., 2009; Pritchard et al., 2009; Seale et al., 2011; Thomas et al., 2009). Yet, the retreat of

these glaciers presents a major barrier in projecting mass loss from the Greenland Ice Sheet due to the highly dynamic and topographically complex glacier-fjord environments (Cowton et al., 2018).

Until recently, glaciers in Northeast Greenland were thought to be relatively stable, with the speedup concentrated in the west, northwest and south of the ice sheet (Kjær et al., 2012; Moon et al., 2012; Pritchard et al., 2009; Rignot et al., 2008). However, observations indicate increased melting in recent years, attributed to anthropogenic climate change (Helm et al., 2014; Mougnot et al., 2019). Some studies have found a positive correlation between ocean temperatures and the terminus position of marine terminating glaciers around Greenland (Cowton et al., 2018; Khazendar et al., 2019).

The Northeast Greenland Ice Stream (NEGIS) is one of the largest ice streams in Greenland, draining approximately 12% of the ice sheet, and stretching back 700 km into its interior (Khan et al.,

* Corresponding author.

E-mail addresses: joannadavies@geo.au.dk (J. Davies), mss@geo.au.dk (M.-S. Seidenkrantz).

2014). The NEGIS is made up of three marine-terminating glaciers: Nioghalvfjærdsbræ (79NG), Zachariae Isstrøm, and Storstrømmen Gletscher. After a period of stability, observations show that the Zachariae Isstrøm retreat began accelerating in the year 2000, resulting in the collapse of its floating ice shelf between 2002 and 2003 (Khan et al., 2014). The Zachariae Isstrøm then entered a period of steady retreat until late 2012, when the floating ice tongue disconnected, and between 2013 and 2014 rapid calving at the grounding line occurred (Khan et al., 2014; Mouginit et al., 2015). Satellite images reveal that the ice shelf decreased from 706 km² in 1985 to 37 km² in 2014; the ice tongue then retreated by 1.6 km between 2014 and 2019, leaving almost no floating section (An et al., 2021). It is hypothesised that these changes can be partly attributed to basal melting, caused by a warming of subsurface waters, namely Atlantic Water (AW) (Holland et al., 2008; Rignot and Mouginit, 2012).

A recent study found that AW controlled 49% of the mass loss from 74 glaciers in deep fjords in Greenland; warming increased undercutting by 48% (Wood et al., 2021). Observations (1996–1997 and 2009) show that AW sits at the mouth of the NEGIS, allowing access to the base of marine-terminating glaciers (Mayer et al., 2000; Rignot and Mouginit, 2012). Given the attribution of warming AW to recent glacial melt, understanding longer-term interactions on the Northeast Greenland continental shelf is key to making projections of future ice retreat. Our understanding of the forces governing ice dynamics is based on complex model simulations and recent observations, constrained by the length of instrumental and observational records. Proxies preserved in marine sediment cores provide records of past climatic and oceanic changes, offering a means to understand ice and ocean dynamics on longer timescales.

The Holocene (11.65 ka – present) is characterised as a period of relative climate stability, compared to the Earth's geological past. However, it encapsulates prominent periods of temperature change. This includes the transition from the Younger Dryas (12.9–11.7 ka) to the Holocene Thermal Maximum, when Greenland summer air temperatures were between 2 and 4 °C warmer than present (Axford et al., 2013; Fréchette and de Vernal, 2009). The timing and magnitude of the Holocene Thermal Maximum differs around Greenland (Axford et al., 2013); it is not well defined in Northeast Greenland. The Holocene also encapsulates the transition from warmer (Holocene Thermal Maximum) to colder conditions (late Holocene, 4.2 ka – present), termed the Neoglacial cooling (Marcott et al., 2013). As a result, the Holocene presents a potential analogue to assess the future effects of anthropogenic climate change on the Greenland Ice Sheet.

¹⁰Be ages suggest that deglaciation on the Northeast Greenland continental shelf to the present ice margin occurred between 11.7 ± 0.6 and 9.3 ± 0.4 ka cal BP; this coincides with an increase in subsurface ocean and air temperatures (Larsen et al., 2018). In fact, datasets indicate a strong inflow of AW (150–800 m), across the Northeast Greenland Shelf during the Early Holocene (10–7.5 ka) culminating in the collapse of a floating ice shelf at ~7.5 ka (Syring et al., 2020a). Radiocarbon dates suggest that the NEGIS was ~20–70 km behind its current extent between ~7.8–1.2 ka cal BP (Larsen et al., 2018). When compared to other major outlet glaciers in Greenland (Hughes et al., 2012), the marine parts of the NEGIS experienced only moderate rates of retreat during the Holocene; this is attributed to the buttressing effect of an ice shelf or sea ice (Amundson et al., 2010; Larsen et al., 2018). Our understanding of the interaction of AW and the glaciers of the NEGIS throughout the Holocene remain poorly constrained due to a lack of regional records.

Low sea ice conditions allowed the collection of numerous marine sediment cores from the inner coast of Northeast Greenland

from the Danish research vessel *DANA*, as part of the North-Green2017 expedition. This included the Gravity Core DA17-NG-ST08-092G, hereafter 92G (585 cm sediment recovered, 78°30.054'N, 16°16.711'W, at 583 m water depth), which is presented in this study. This site is of great interest in assisting with our understanding of the interaction between AW on the Northeast Greenland continental shelf and the NEGIS. Detailed analysis of biological (benthic foraminifera), chemical (XRF, stable isotopes) and physical (grain size data, CT scans) proxies were undertaken on the core, to reconstruct changes in ocean circulation patterns and the timing of the retreat and collapse of the NEGIS throughout the Holocene.

1.1. Regional setting

The study area is located on the Northeast Greenland continental shelf to the east of the NEGIS; today the Zachariae Isstrøm is the closest marine terminating glacier to our core site (Fig. 1A). The Northeast Greenland continental shelf is approximately 300 km wide and is characterised by a 'C'-shaped trough system, made up of the Norske and Westwind troughs (Fig. 1B). These troughs converge in a 250 m deep sill near the margin of the NEGIS at about 79.58°N (Budéus et al., 1997; Schaffer et al., 2020; Straneo et al., 2012). The exact core site is located on the inner continental shelf, in the Norske Trough, at 583 m water depth (Fig. 1B). The Norske Trough is 350 km long; it increases from a width of 35 km to a maximum of 200 km. Today, the Norske Trough has reverse slopes, which are similar to deep troughs present in other regions formerly covered by the ice sheet (Arndt et al., 2015; Batchelor and Dowdeswell, 2014).

Northeast Greenland is characterised by the interaction and movement of Polar Water (PW) at the surface and the underlying AW (Fig. 1A). The PW is formed by cold (0–1 °C), low-saline (<34.5) surface waters from the Arctic Ocean and local meltwater from the Greenland Ice Sheet; it occupies the uppermost 250 m of the water column (Aagaard and Coachman, 1968; Hopkins, 1991; Johannessen, 1986). The East Greenland Current carries the PW southwards along the eastern coast of Greenland over the continental shelf. AW lies at subsurface water depths; it is made up of Return Atlantic Water and Arctic Atlantic Water (Rudels et al., 2005). The West Spitsbergen Current carries AW northwards; around half is deflected westwards forming the Return Atlantic Current, which transports Return Atlantic Water (T < 2 °C, S: 34–35) towards Northeast Greenland, where it mixes with the PW of the upper East Greenland Current (de Steur et al., 2014). The eastern branch of the West Spitsbergen Current travels northwards to the Arctic Ocean, where it cools and freshens and merges with AW that travelled via the east coast of Svalbard (Rudels et al., 1994). Now termed Arctic Atlantic Water, it circulates in the Arctic Ocean before exiting through the Fram Strait to join the Return Atlantic Water at 78°N (Schaffer et al., 2017). Together the Return Atlantic Water and Arctic Atlantic Water form the Atlantic Intermediate Water (150–800 m) (de Steur et al., 2014; Rudels et al., 2012). Whilst much of the Atlantic Intermediate Water is carried by the East Greenland Current southwards along the outer shelf edge, some enters the inner shelf via deep channels and troughs towards the NEGIS. In this paper, we do not distinguish between the sources of paleo-Atlantic-source water and thus collectively refer to it as AW.

The Westwind and Norske troughs provide deep pathways for AW to enter cavities on the ice shelf beneath marine terminating glaciers (Arndt et al., 2015); the Zachariae Isstrøm is located at the western end of the Norske Trough. The Norske and Westwind troughs are mainly dominated by Return Atlantic Water and Arctic Atlantic Water respectively (Fig. 1B; Schaffer et al., 2017). Seafloor

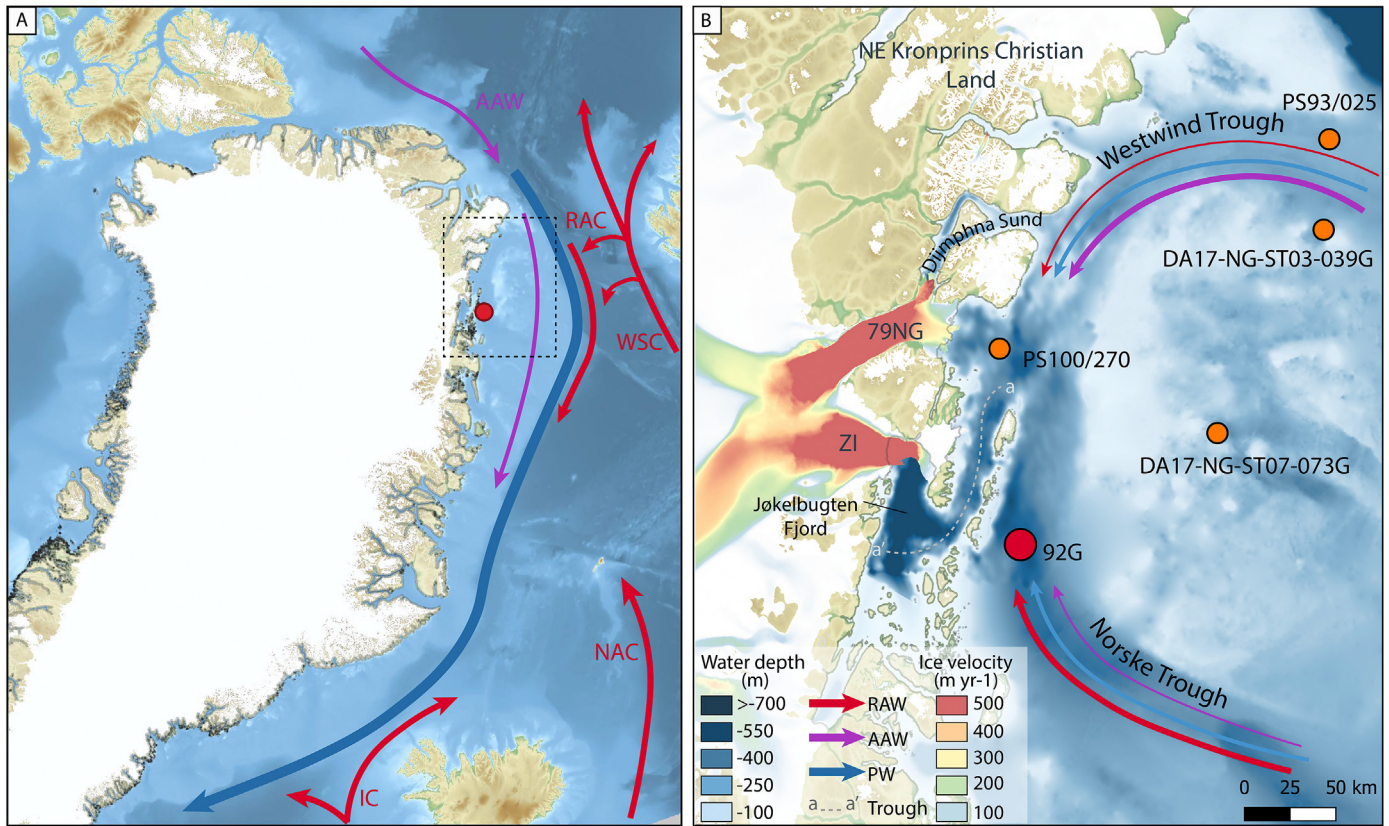


Fig. 1. A) Overview of the study site ocean circulation patterns: the warm currents which include the Return Atlantic Current (RAC), West Spitsbergen Current (WSC), North Atlantic Current (NAC), Irminger Current (IC) (red), the Polar Water (PW) carried by the East Greenland Current (EGC) (blue) and Arctic Atlantic Water (AAW) (purple). 92G is shown (red circle). The ocean bathymetry is from GEBCO Compilation Group (Weatherall et al., 2015), B) Close up of the Northeast Greenland continental site showing the cores discussed here; 92G (red) and other cores (orange): PS100/270 (Syring et al., 2020a), DA17-NG-ST03-039G (Hansen et al., in review), DA17-NG-ST07-073G (Pados-Dibattista et al., 2022) and PS93/025 (Syring et al., 2020b; Zehnich et al., 2020) local bathymetry and topography, and glaciers that make up the NEGIS: Zachariae Isstrøm (ZI) and Nioghalvfjærdsfjorden Glacier (79NG). The strength of currents is shown by the line thickness. Line a-a' represents the 370–500 m deep trough which connects the Norske Trough to the Jøkelbugten fjord (Yang et al., 2020). The ocean bathymetry is from Arndt et al. (2015) and Yang et al. (2020) and ice stream velocity data come from Sentinel- SAR data from 2019–2020 (Nagler et al., 2015). (For interpretation of the references to colour in this figure legend, the reader is referred to the Web version of this article.)

topography has recently been inferred from airborne gravity using a nonlinear inversion; it revealed a 370–560 m deep trough that connects the Norske Trough to the Jøkelbugten fjord in which the Zachariae Isstrøm drains; this allows entry of AW (Fig. 1B, line a-a'; Yang et al., 2020). Modern measurements support this, indicating that AW enters the Norske Trough and reaches the inner fjords and calving front of the Zachariae Isstrøm. The influx of AW is thought to have a great influence on the coastal glaciers in the area (Schaffer et al., 2017).

2. Materials and methods

2.1. Core collection and CTD

The multi-proxy dataset presented in this study is derived from Gravity Core DA17-NG-ST08-092G collected in September 2017 onboard the research vessel *DANA* as part of the NorthGreen2017 expedition (Seidenkrantz et al., 2018). The 585 cm long core was collected at 583 m water depth on the Northeast Greenland continental shelf (78°30.054'N, 16°16.711'W), 90 km east of the Zachariae Isstrøm terminus. After retrieval, the core was cut into 1 m sections, split and stored at 3 °C at Aarhus University, where it was subsampled for analysis. A 125 cm Rumohr core, DA17-NG-ST08-90R (hereafter 90R; 78°30.001'N 17°18.431'W), was retrieved at the same station from 595 m water depth. Comparison between these cores indicates that 9 cm of sediment was lost from the top of

92G; apart from this, no sediment was lost during the coring process (Supplementary Fig. 2). Temperature and salinity data, as a function of depth, was collected using the Seabird SBE11 CTD (cast DA17-NG-ST08-084CTD; 78°29.616'N, 17°21.609'W, 595 m water depth). A shallow seismic survey was undertaken using an Innomar SES-2000 Deep, Narrow-Beam Parametric Sub-Bottom Profiler prior to core collection to assist in selecting suitable sediments.

2.2. Physical properties and lithology

The colour, structure and grain size of the sediment core was described soon after collection, using a Munsell colour chart. Grain size analysis was carried out on a Sympatec HELOS laser diffractometer, equipped with a Quixel wet disperser, 6 mm cuvette and R4 lens, at 1 cm intervals throughout the entire core at the Department of Geoscience, Aarhus University. Peptizer solution (10 ml (NaPO₃)₆ 15%) was first added to the laser diffractometer and a reference measurement undertaken. The sample was then fed into the laser diffractometer for measurement. The average of 3–5 measurements for each sample was calculated. For interpretation, grain sizes are grouped into: sand (>63 µm), medium to coarse silt (15.6–63 µm), very fine to fine silt (3.9–15.6 µm) and clay (0.6–3.9 µm). Mean grain size between 10 and 63 µm was grouped as mean sortable silt (\bar{S}) to reconstruct the speed of bottom water currents (McCave et al., 1995); it assumes that bottom currents

cannot carry terrestrial sand-sized material. The fraction between 2 and 10 μm is excluded as small particles tend to aggregate, effectively acting as a larger particle. At high latitudes, sediments typically contain particles derived from ice-rafting together with current transport material. Whilst IRD typically contains particles within the sand and gravel fraction it can also contain material in the SS fraction (Hass, 2002). However, a regression between the IRD (grains >3 mm) and \overline{SS} suggests there is no or very little correlation between the two (Supplementary Fig. 1). As a result, \overline{SS} is used here without need for correction.

2.3. CT scanning

The computed tomography (CT) data was acquired using a Siemens Biograph True Point 64 medical PET/CT scanner at the Department of Nuclear medicine & PET, Aarhus University Hospital. The CT scan parameters were: 120 kV, 400 Eff mAs, 200 mm field of view, slice thickness 0.6 mm, filter B80s (sharp), and gantry rotation speed of 1 s. A current of 400 mA and a voltage of 120 keV was used at a gantry rotation speed of 1 s. Each core section was placed top first in the CT scanner. The resulting CT images (approximately 1800 per section) were then imported into the image editing software Fiji and the mean Hounsfield units (HU) value (1024) extracted (Rueden et al., 2017). The HU units can be used to calculate an estimated density of the sediment using the following equation (Reilly et al., 2017):

$$\text{Density} \left(\frac{\text{g}}{\text{cm}^3} \right) = 8.0 * 10^{-4} * \text{HU} + 1.00$$

The CT images were visually examined to identify laminations, IRD and bioturbation to define lithofacies using the image editing software Fiji (ImageJ2) (Rueden et al., 2017). Grains >3 mm were counted at 2 cm resolution; these were used to assist in the identification of IRD in the bioturbated sections of the core (Grobe, 1987). The close proximity of the ice grounding line to our site, characterised as laminations within the sediment, makes it difficult to distinguish the difference between IRD and sediment plumes. Consequently, in laminated sediment IRD is identified as exotic grains that are more than double in size of those around them and that are not located within defined laminae.

2.4. X-ray fluorescence

The sediment core was scanned by X-ray fluorescence (XRF) with an ITRAX scanner equipped with a Molybdenum X-ray tube at 30 kV and 30 mA to record the elemental spectra at 0.2 mm resolution, at the Department of Geoscience, Aarhus University. A 2 cm running average was calculated to reduce noise for analysis. High-resolution core scans and radiograph images (30 kV) were also collected using the ITRAX core scanner. The magnetic susceptibility was measured (5 mm resolution) using a Bartington MS2 fitted within the ITRAX core scanner.

2.5. Chronology

The age model for core 92G is based on 16 radiocarbon dates obtained from 10 mixed rotaliid benthic and 5 mixed planktic foraminiferal samples, as well as a shell fragment analysed at the Laboratory of Ion Beam Physics at ETH Zurich (Ruff et al., 2010; Wacker et al., 2013a, 2013b). Planktic foraminiferal radiocarbon dates are used in the model, except when there are no specimens present; in these instances benthic foraminiferal samples are used. Samples containing more than 40 μg carbon were leached prior to the analysis with diluted HCl (Bard et al., 2015). The measured leach

fractions were always in good agreement with the corresponding main fractions indicating that samples from this core were clean and homogeneous. The radiocarbon ages were calibrated using the Marine20 radiocarbon calibration curve (Heaton et al., 2020) and the age-depth model made using the OxCal v4.4 software with a *P*-sequence depositional model (k value 0.1). Heaton et al. (2020) state that Marine20 is not suitable for use in the Arctic, however the earlier version (Marine13; Reimer et al., 2013) is not suitable either, yet is commonly used in this region (e.g. Perner et al., 2015; Syring et al., 2020a). The reason for this statement is sea ice, which creates uncertainty with the reservoir age. However, this uncertainty is not resolved by using an older version of the calibration dataset (e.g. Marine13). Consequently, many studies still use Marine20 in Arctic regions (e.g. Farmer et al., 2021; El bani Altuna et al., 2021; Pados-Dibattista et al., 2022; Jackson et al., in review), and thus we select it for use in this study.

A boundary for the change in sedimentation rate is placed at 67 cm, determined by a shift in sediment lithology visible in the CT scans. A regional marine reservoir correction of $\Delta R = 1 \pm 32$ years, obtained from the Marine Reservoir Correction Database (Reimer and Reimer, 2001) and based on references from the region (Håkansson, 1973; Funder et al., 1982), was used for the calibration of radiocarbon dates in this study. ΔR is kept constant for the entire period. XRF and grain size data was used to correlate Rumohr Core 90R and Gravity Core 92G to determine the amount of sediment lost during gravity coring.

2.6. Foraminifera

Sediment samples (1 cm wide) of approximately equal volume were extracted at 5 cm intervals throughout the core. Due to varying sedimentation rates, the temporal resolution changes throughout the core. For foraminiferal analysis, resolution varies from 0.9 mm/yr to 1.6 mm/yr in most of the core (585 cm–60 cm), while at the top of the core it is 0.08 mm/yr (60 cm–0 cm). The wet sediment was weighed and sieved with 0.063, 0.1 and 1 mm mesh sizes, respectively. The sieved sample fractions were dried in filter paper at 40 °C, weighed and then stored in glass vials. Benthic and planktic foraminifera were identified and counted under a binocular microscope. When possible, at least 300 benthic (combined calcareous and agglutinated) were counted to ensure reliability of the benthic assemblage interpretation. However, some samples had few specimens, these are only included when at least 30 specimens were present. Fractions 0.063–0.1 mm and 0.1–1 mm were counted separately on trays, and ratios calculated afterwards to ensure proportions were directly comparable prior to combining the data. Concentrations of benthic (agglutinated and calcareous) foraminifera were calculated as number of specimens/cm³ sediment. The flux of benthic foraminifera was calculated based on the number of individuals per cm³ of sediment (ind./cm³) and sedimentation rate (cm/yr).

2.7. Stable isotopes

Stable isotope ratios $\delta^{13}\text{C}$ and $\delta^{18}\text{O}$ were measured on mono-specific *Cassidulina neoteretis* foraminifera at 5 cm or 10 cm resolution between 65.5 cm and 375.5 cm, with a temporal resolution of between 0.4 mm/yr and 1.6 mm/yr due to varying sedimentation rates. Analysis was undertaken at the Leibniz Laboratory for Radiometric Dating and Stable Isotope Research, University of Kiel, Germany using a MAT25 (Thermo specific) mass spectrometer system and Kiel IV carbonate preparation device. The analytical accuracy is < 0.08‰ for $\delta^{18}\text{O}$ and < 0.05‰ for $\delta^{13}\text{C}$.

3. Results

3.1. CTD and water masses

The local surface water (upper 25 m) at the core site has a temperature range of $-1.25-0\text{ }^{\circ}\text{C}$ and salinity of 28.5 (Fig. 2A). This surface temperature range is similar to those recorded at 79.5°N , 19°W ($-1.75-0\text{ }^{\circ}\text{C}$) (Schaffer et al., 2017). The water that underlies the surface water, between 25 m and 125 m, is the PW component of the East Greenland Current, which has temperatures between $-1\text{ }^{\circ}\text{C}$ and $-1.6\text{ }^{\circ}\text{C}$ and salinities of 31–34. Beneath this is a layer where the water is characterised by increasing temperatures with depth: from $1\text{ }^{\circ}\text{C}$ to a maximum of $1.5\text{ }^{\circ}\text{C}$ (Fig. 2A), caused by the mixing of PW and AW. The deepest water (below 270 m) is the warmest ($1.5-1.4\text{ }^{\circ}\text{C}$) with the highest salinities (35) and corresponds to the subsurface AW, comprising Arctic Atlantic Water and Return Atlantic Water (Fig. 2B; de Steur et al., 2014).

3.2. Core description, lithology and sediment properties

The core primarily consists of reddish-brown (5 YR 5/3) fine-grained clay. Photographs and CT scans (Fig. 3A) reveal six main sediment lithofacies: a possible diamicton, laminations with coarser grains, laminations with finer grains, laminations with IRD, bioturbation with IRD and bioturbation without IRD (Fig. 3C). A detailed overview of the CT scans can be found in Supplementary Fig. 3. The base of the core (585–582 cm) is characterised by coarse-grained sediments with a large dropstone at the base; this is also visible as spikes in the density. The lower section (582–300 cm) is characterised by intervals of light-coloured laminae made up of finer grains, also clearly visible in the CT scans, interrupted by a short period with bioturbation and IRD (358–311 cm) corresponding to an increase in magnetic susceptibility, before the sediment returns to laminations with finer grains and the density drops (311–160 cm) (Fig. 3A). The upper part of the core (160–0 cm) is characterised by homogenous reddish-brown clay with bioturbation; some IRD is present between 51 and 68 cm (Fig. 3A).

Five zones have been defined by a visual interpretation of sediment properties and benthic foraminiferal assemblages; boundaries are placed where changes in the assemblage composition and sediment properties occur.

3.3. Age-depth model

Radiocarbon dates from foraminifera (benthic and planktic) and the shell sample from core 92G are shown in Table 1. The age-depth model is shown in Fig. 3B. The nearby-located Rumohr Core 90R was retrieved with an intact sea-floor sediment surface; we assume that the surface is modern. When grain size and XRF data from 90R to 92G are aligned it shows that the gravity core is missing approximately 9 cm of material (Supplementary Fig. 2). Where there is an offset between paired dates, the planktic dates are selected and the benthic dates excluded. There are several other dates that are excluded from the age model (361 cm, 470.5 cm) as the ages were older than the surrounding samples. This may be due to the small sample sizes, or due to older material that is potentially transported into the sediment; in a small sample such material can have a strong effect. The age model indicates that core 92G covers the last 13.4 kyr.

3.4. Sedimentation rate and grain size

The sediment accumulation rate is relatively high (110 cm/kyr) in the Early Holocene, increasing to its maximum rate (160 cm/kyr) at 10.8 ka cal BP. The sedimentation rate decreases at 9.4 ka cal BP (50 cm/kyr), before reaching its lowest rate at 7.3 ka cal BP (ca. 8 cm/kyr) in the upper ca. 60 cm of sediments. \overline{SS} fluctuates between 13.4 and 8.8 ka cal BP, with some distinct peaks, it then gradually declines from towards its lowest value in the top of the core (Fig. 4).

The sediment grain size is dominated by the clay fraction throughout the core (Fig. 4). The sand fraction fluctuates in the lower part of the core, with noticeable peaks in the base. After 8 ka cal BP, the sand fraction is almost completely stable and found in its lowest abundance throughout the entire core. The silt fraction (medium to coarse) is relatively stable throughout the core, with most fluctuations found before 8.6 ka cal BP (Fig. 4). Throughout the remaining part of the core, this fraction is very stable. The silt (very fine to fine) and clay fractions appear to be frequently inversely correlated; the most noticeable transition is the gradual increase in silt (very fine to fine) and decline in clay from 8.8 ka cal BP.

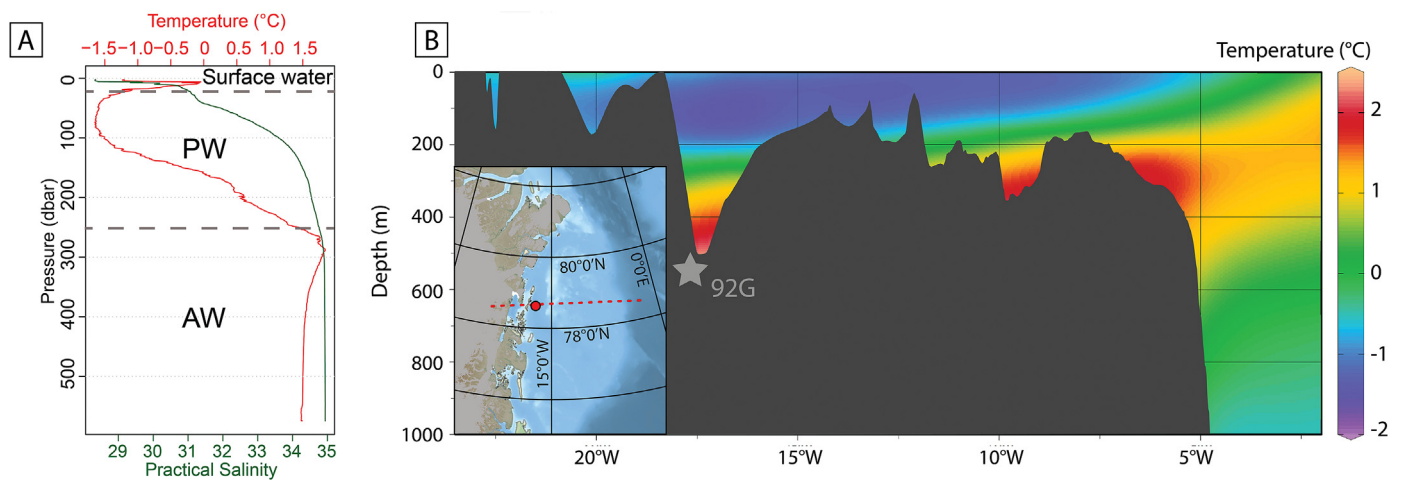


Fig. 2. A) The CTD profile (cast DA17-NG-ST08-084CTD) from the core site of 92G, showing the water masses referenced in the text. B) Annual average water temperature transect at 78.5°N showing water masses at the study site. Temperature data from World Ocean Atlas (2018) (Locarnini et al., 2018) and bathymetry from (Arndt et al., 2015) from the transect (red dotted line). The location of core 92G is shown (grey star). (For interpretation of the references to colour in this figure legend, the reader is referred to the Web version of this article.)

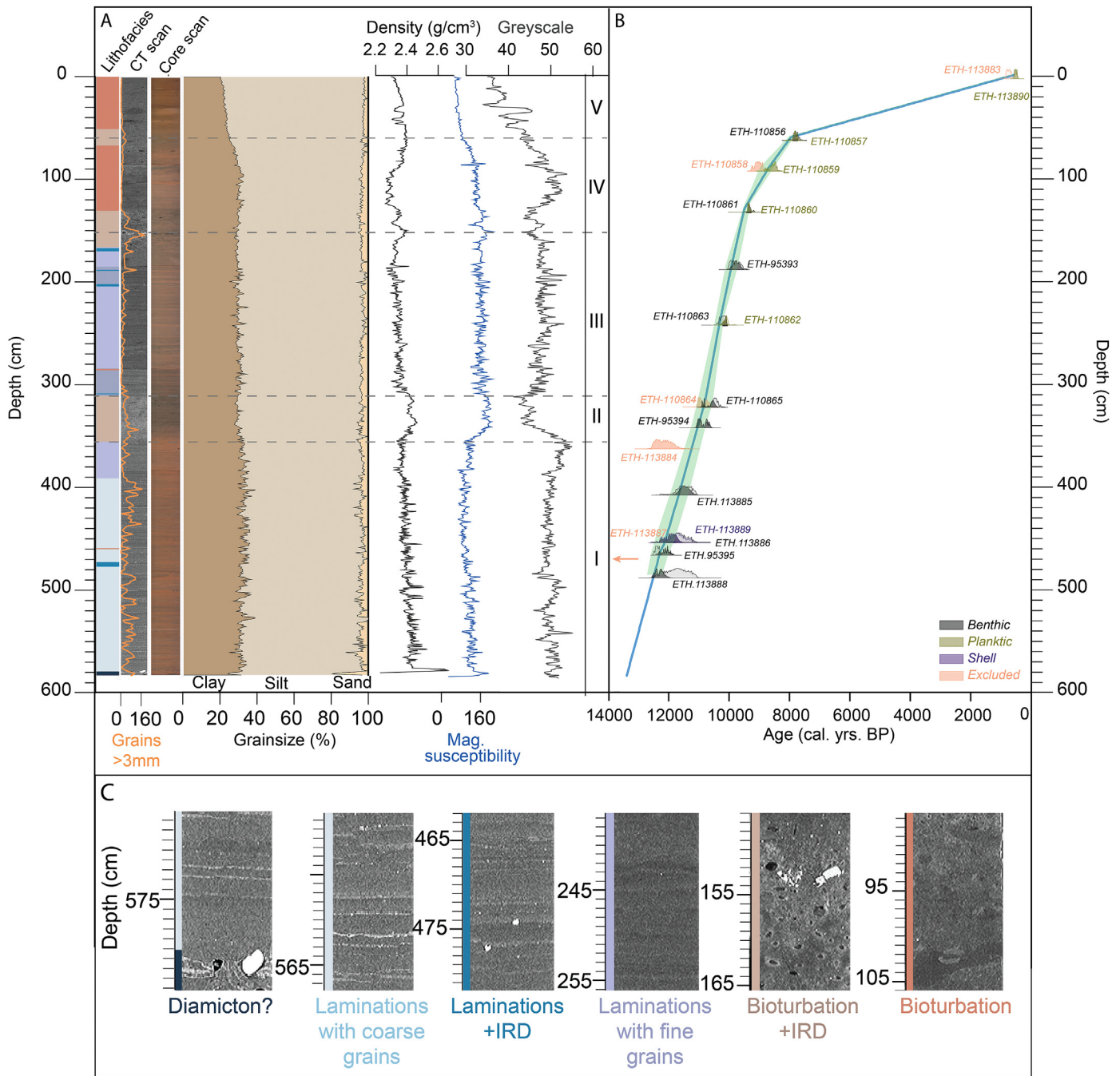


Fig. 3. Lithology and age-model of Gravity Core 92G. A) High -resolution scans and CT images, with the sediment units categories with counts of grains >3 mm (orange). The grain size distribution (clay, silt and sand), density, magnetic susceptibility, greyscale are plotted. Zones are shown on the right hand side. B) Age-depth model with planktic foraminifera dates (green), benthic foraminifera (black) a shell fragment (indigo). Dates not included in the age-depth model are plotted (light salmon). The top of the core has been aligned with Rumohr Core 90R. The modelled median age is shown (blue line), and is surrounded by the 2σ modelled range (light green envelope) C) Lithofacies defined using CT scans and counts of grains >3 mm, (from left to right) potential diamicton (dark blue), laminations with coarse grains (light blue), laminations with IRD (blue), laminations with fine grains (purple), bioturbation with IRD (light pink) and bioturbation (dark pink). (For interpretation of the references to colour in this figure legend, the reader is referred to the Web version of this article.)

3.5. XRF

Bulk chemical ratios are primarily used to identify the source of sediments, specifically whether they are of marine or terrestrial origin (Fig. 4). Ca/Fe is highest between 13.4 and 7.9 ka cal BP, and decreases gradually thereafter. In the lower part of the core there are some fluctuations and noticeable peaks.

3.6. Stable isotopes

Generally seen, the $\delta^{13}\text{C}$ and $\delta^{18}\text{O}$ are stable throughout the measured interval of the core since the variations vary within 1 per mil VPDB (Fig. 4). There is a slight overall increasing trend in the $\delta^{18}\text{O}$ from 9.3 ka cal BP. The $\delta^{13}\text{C}$ appears quite stable, but with small fluctuations.

Table 1

List of radiocarbon dates and modelled ages in core 92G; the modelled dates are used in the final age-depth model. Samples marked with * were very small and could not be leached.

Sample depth midpoint (cm)	Lab ID (ETH)	Material	¹⁴ C Age (yr. BP)	Unmodelled calibrated age range (yrs. BP) 2σ	Modelled median age (cal yrs BP)
0.5	113890	Mixed planktic foraminifera	595 ± 50	528–657	597
0.5	113883	Mixed benthic foraminifera	920 ± 60	695–953	
60.5	110856 *	Mixed benthic foraminifera	7120 ± 80	7752–8166	
60.5	110857	Mixed planktic foraminifera	7130 ± 60	7793–8156	7946
90.5	110858	Mixed benthic foraminifera	8220 ± 70	9012–9414	
90.5	110859	Mixed planktic foraminifera	7865 ± 60	8540–8984	8670
130.5	110861 *	Mixed benthic foraminifera	8495 ± 80	9293–9659	
130.5	110860	Mixed planktic foraminifera	8505 ± 70	9310–9658	9495
186.5	95393 *	Mixed benthic foraminifera	8855 ± 70	9687–10189	9919
240.5	110863	Mixed benthic foraminifera	9195 ± 70	10232–10560	
240.5	110862 *	Mixed planktic foraminifera	9090 ± 70	9967–10496	10284
320.5	110864 *	Mixed benthic foraminifera	9680 ± 70	10774–11235	
320.5	110865 *	Mixed planktic foraminifera	9400 ± 70	10410–11067	10748
340.5	95394 *	Mixed benthic foraminifera	9710 ± 80	10773–11255	11043
361	113884 *	Mixed benthic foraminifera	10480 ± 160	11834–12737	
406	113885 *	Mixed benthic foraminifera	10080 ± 120	11240–12425	11640
451.5	113886 *	Mixed benthic foraminifera	10180 ± 120	11336–12466	12074
452.5	113889 *	Shell fragment	10220 ± 130	11355–12480	12062
464.5	95395 *	Mixed benthic foraminifera	10490 ± 270	12099–12688	12261
470.5	113887 *	Mixed benthic foraminifera	21890 ± 380	25389–27163	
486.5	113888 *	Mixed benthic foraminifera	10200 ± 190	11268–12595	12473

3.7. Foraminifera and zonations

In general, benthic foraminiferal specimens (agglutinated and calcareous species) are well preserved throughout the core. In total, 97 benthic foraminiferal species were identified, 75 calcareous and 22 agglutinated; species with 4% abundance in at least one sample are shown (Fig. 5). A full list of the foraminiferal taxa identified in this study can be found in Supplementary Table 1. Fluxes of benthic and planktic species were calculated using the number of individual species per cm³ of sediment (ind.cm³) and the sedimentation rate (cm/yr). The relative abundances of calcareous and agglutinated benthic foraminiferal assemblages are calculated based on the combined counts, as the agglutinated species exclusively dominate the sediment from 7.9 ka cal BP. Concentrations of the selected species can be found in Supplementary Fig. 4.

The following section provides a detailed overview of the zonal changes in foraminifera, with additional detail from the CT scans in some instances as they are used for zone identification.

3.8. Zone I, 13.4–11.2 ka cal BP

This zone is characterised by a low concentration of benthic foraminifera, first appearing at 13.1 ka cal BP, accompanied by a relatively high sedimentation rate and distinct laminations throughout. Agglutinated foraminifera are almost absent throughout this entire zone and the assemblage is dominated by *C. neoteretis*, *Cassidulina reniforme*, and *Stetsonia horvathi*; these fluctuate slightly throughout. *C. neoteretis* gradually increases towards the end of the zone. The abundance of *Glomulina oculus* and *Stainforthia concava* peaks at the start of the zone and then declines sharply, followed by some fluctuations. The abundance of *Miliolinella subrotunda*, *Quinquolucina* sp. and *Triloculina trihedra* fluctuate throughout, but are present in higher concentrations than the rest of the core. *Melonis barleeanus* noticeably appears during the middle-later part of the zone. The agglutinated species *Ammoglobigerina globigeriniformis* and *Portatrochammina bipolaris* also appear in this zone, fluctuating in low numbers throughout.

3.9. Zone II, 11.2–10.8 ka cal BP

This brief interval is characterised by bioturbation with IRD, coinciding with an increase in the total foraminiferal concentration and a very slight increase in agglutinated species. As for the previous zone, the assemblage is dominated by *C. neoteretis*, *C. reniforme* and *S. horvathi*; these fluctuate slightly throughout. There is a peak in *C. neoteretis* at the start of the zone and *Islandiella norcrossi* peaks dramatically towards the end of the zone (11 ka cal BP), reaching its highest abundance throughout the entire core (12%). This coincides with a large peak in *G. oculus*. The abundance of *C. reniforme*, *Elphidium clavatum* and *S. horvathi* remain relatively constant throughout, with some small fluctuations. This zone is also characterised by a sudden decline in *M. subrotunda*, *Quinquolucina* sp. and *T. trihedra*, which remain relatively low throughout the entirety of this zone.

3.10. Zone III, 10.8–9.6 ka cal BP

After the short period of bioturbation, this zone is characterised by a return to laminated sediments. This coincides with a decline in the overall foraminiferal concentration and by the fluctuating dominance of *C. neoteretis*, *C. reniforme*, and *G. oculus*, which gradually increase throughout the zone. The overall abundance of *E. clavatum*, *S. concava*, and *M. barleeanus* remain low, if not almost absent, throughout this entire zone. Following the peak in *I. norcrossi* at the end of Zone II/start of Zone III, the species abundance declines and fluctuates throughout the rest of the zone. *G. oculus* is noticeably more abundant following its peak at the end of Zone II. *Alabaminella weddellensis* appears, following a period of almost absence. There is a slight increase in agglutinated species *A. globigeriniformis* and *P. bipolaris* towards the top of the zone.

3.11. Zone IV, 9.6–7.9 ka cal BP

Zone IV is characterised by a gradual increase in the total foraminiferal concentration, peaking at 8.1 ka cal BP. This coincides with the increase in *E. clavatum*. *C. neoteretis* is abundant throughout the zone, before dramatically decreasing towards the

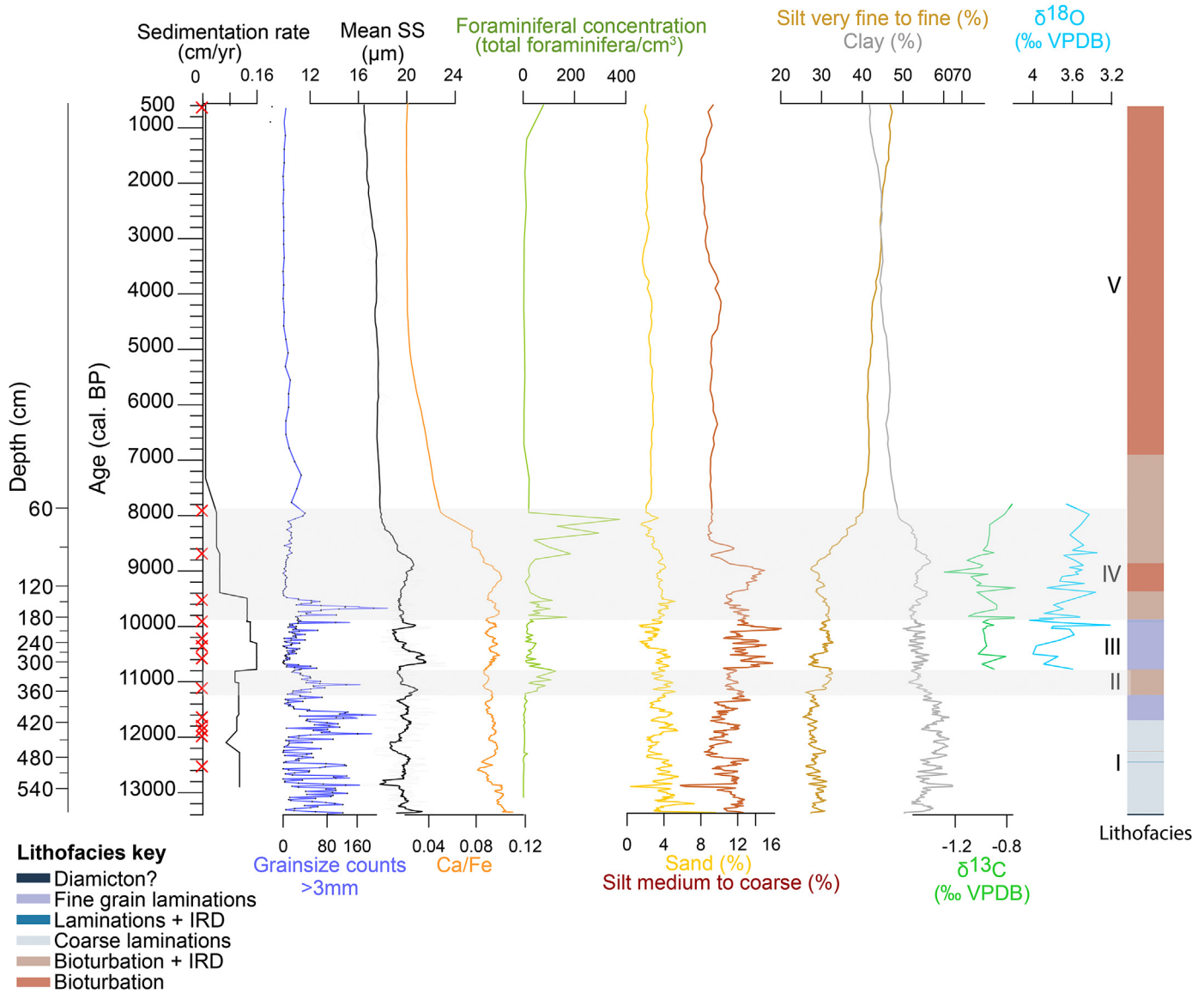


Fig. 4. Sedimentation rate, grain>3 mm, Ca/Fe, foraminiferal concentration, and the grain size distribution (from left to right: sand, silt (medium to coarse), silt (very fine to fine) and clay), and stable isotope ratios on *Cassidulina neoteretis* for marine sediment core 92G. Radiocarbon dates (red crosses), zones (grey; right) and lithofacies determined from CT scans (right) are also shown. (For interpretation of the references to colour in this figure legend, the reader is referred to the Web version of this article.)

end. There is a continued presence of *M. barleeanus*, *Epistominella takayanagii* and *A. weddellensis*, with the latter two increasing towards the end of the zone. *Cibicides* sp. and *Astronion gallowayi* are also present, yet fluctuating, throughout. *G. oculus* disappears in the middle of this zone (8.4 ka cal BP). This coincides with a return to bioturbated sediments for the remainder of the core.

3.12. Zone V, 7.9–0.6 ka cal BP

The start of this zone is characterised by a rapid decline in the total foraminiferal concentration and increase in the overall percentage of agglutinated species. This coincides with a dramatic decline in calcareous species; most noticeably in *C. neoteretis* and *I. norcrossi*. There is a gradual decline in *S. horvathi*, and *C. reniforme*. At the same time, peaks in *E. takayanagii* and *A. weddellensis* are accompanied by larger peaks in *E. clavatum*, *M. barleeanus*, and *A. gallowayi*; it should be noted that the temporal resolution is

lower here. The agglutinated assemblage species fluctuate throughout this zone.

The assemblage is primarily dominated by agglutinated species with the most abundant being *Lagenamma* spp., *P. fusca*, *L. tabulate*, *Cribrostomoides subglobosus*, and *P. bipolaris*. There are very few calcareous species present in this subzone. These species fluctuate throughout but there is a distinct increase in *P. bipolaris*, which peaks at 4.2 ka cal BP. The total concentration of foraminifera is low throughout this zone, with calcareous species almost completely absent. *Hormosinelloides guttifer* appears for the first time during this time period.

At 2.5 and 0.6 ka cal BP some calcareous foraminifera appear again, specifically *E. clavatum*, *C. neoteretis*, *I. norcrossi*, *C. reniforme*, *M. barleeanus*, *C. lobulatus*, *Valvulineria arctica*, *Nonionella fragilis*, *Oridorsalis tener*, and *A. gallowayi*. There is a noticeable peak in *O. tener* (12%) and *E. clavatum* (11%). At the same time, there is a peak in the overall concentration of agglutinated foraminifera.

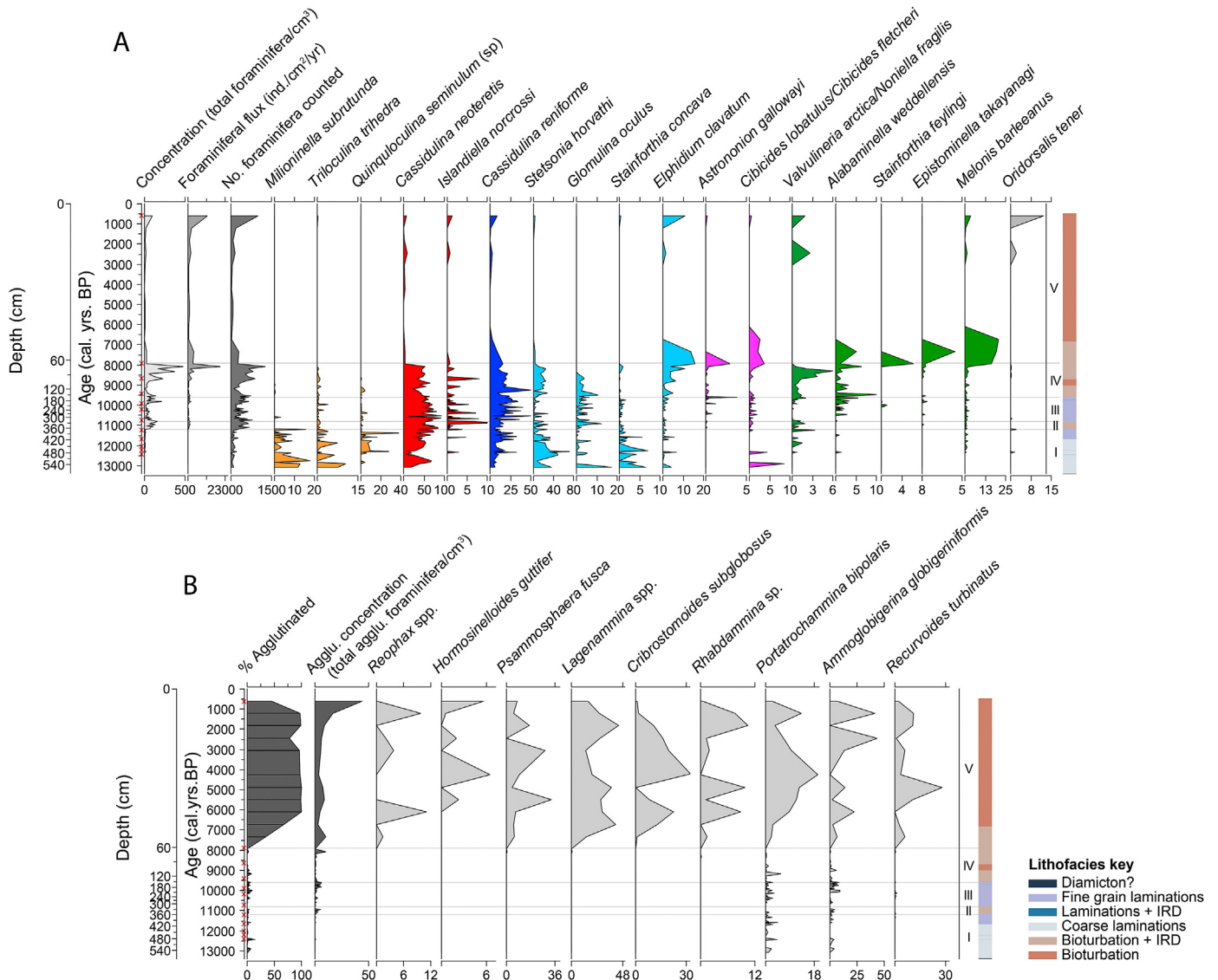


Fig. 5. A) Results of the calcareous and benthic foraminiferal assemblage analysis for core 92G, shown on age and depth. Calcareous foraminifera are grouped by their environmental preferences, see text for reference: Atlantic Water (red), Polar Water (dark blue), glaciomarine (light blue), high productivity (green), high currents (pink), high salinity (orange). B) Results of agglutinated foraminiferal analysis for core 92G, shown on age and depth. Species percentages are calculated as a percentage of the entire assemblage (agglutinated + calcareous species). Radiocarbon dates (red crosses), zonation and lithofacies (right) are shown. (For interpretation of the references to colour in this figure legend, the reader is referred to the Web version of this article.)

4. Paleoenvironmental interpretation

In the Arctic and subarctic, the benthic foraminiferal species *C. neoteretis* and *I. norcrossi* are typically indicators of the inflow of chilled AW, here derived from the Return Atlantic Current and/or Arctic Atlantic Water, which sits below PW (Cage et al., 2021; Jennings et al., 2004; Jennings and Helgadottir, 1994; Knudsen et al., 2004; Seidenkrantz, 1995; Wollenburg et al., 2004). In this instance, we cannot distinguish between the two Atlantic-source water masses so we use both *C. neoteretis* and *I. norcrossi* to infer the presence and advection of AW more generally. Nevertheless, it may be assumed that *C. neoteretis* indicates a stronger AW signal than *I. norcrossi* (Cage et al., 2021).

C. reniforme is typically found in glaciomarine environments, preferring temperatures below 2 °C, with seasonal sea ice cover and often close to the glacier terminus (Hald and Korsun, 1997; Polyak et al., 2002). Similarly, *E. clavatum* is characteristic of unstable,

glaciomarine environments with input of glacial meltwater and high turbidity (Hald and Korsun, 1997). The species *S. horvathi* is characteristic of colder surface waters and more extensive sea ice conditions, also typical of a glaciomarine environment (Jennings et al., 2004, 2020b; Polyak et al., 2002; Wollenburg and Mackensen, 1998). The species *G. oculus* is indicative of environments close to marine terminating glaciers in the Arctic. It often lives beneath perennial or mobile sea ice with a stratified water column with AW overlain by PW (Jennings et al., 2020a).

It is important to consider the possible reasons behind the varying preservation of calcareous foraminifera downcore. The percentage of agglutinated species can be an indicator of calcareous foraminiferal dissolution caused by cold, corrosive waters which increase the solubility of CO₂ (Aksu, 1983; Jennings and Helgadottir, 1994; Seidenkrantz, 2013). As a result, the increasing abundances of the agglutinated species, combined with low fluxes of the calcareous benthic species, are often used to infer a transition towards

colder subsurface water conditions (Aksu, 1983; Jennings and Helgadottir, 1994; Seidenkrantz, 2013). In Disko Bay, calcareous foraminiferal dissolution has also been linked to changing sedimentation rates (Lloyd, 2006; Lloyd et al., 2005, 2007). Close to Jakobshavns Isbrae, calcareous foraminifera are better preserved during periods with high sedimentation rates and are more susceptible to dissolution during periods with a reduced sedimentation rate (Lloyd et al., 2007). Sea ice formation can also reduce bottom water ventilation, resulting in corrosive conditions. This has been proposed as a reason for the dissolution of calcareous foraminifera in Baffin Bay (Aksu, 1983) and Disko Bay (Lloyd et al., 2007). It should, however, be borne in mind that agglutinated species may disintegrate downcore as they are crushed due to increasing pressure stress. Fossils of agglutinated species often decrease downcore (Funder, 1990) and thus it is not directly the presence of agglutinated foraminifera but the absence of calcareous foraminifera that is relevant when considering potential dissolution.

Ca/Fe is frequently used as an indicator of biologically sourced carbonate, yet it can be masked by terrestrially sourced Ca (Richter et al., 2006). It is therefore used together with the foraminiferal concentration to determine the sources of biologically sourced carbonate. Stable isotopic composition of benthic foraminiferal tests, $\delta^{13}\text{C}$ and $\delta^{18}\text{O}$, are used to suggest changes in productivity and temperature respectively; low ^{18}O values ($\sim 4\text{‰}$) in benthic foraminifera infer low temperature and high salinity bottom waters (Ouellet-Bernier et al., 2014).

The distribution of grain sizes can be used to infer the sources and transport mechanisms by which they were carried to our site, such as ice rafting and ocean currents (Stein et al., 2004). The lithofacies and sedimentation rate are used to infer the proximity of the NEGIS; laminated sediments are often characteristic of a proximal glaciomarine environment, produced by suspension settling from turbid meltwater plumes (Ó Cofaigh and Dowdeswell, 2001; Stein, 2008; Syring et al., 2020a; Jennings et al., 2022). IRD, visible in the CT scans, are used to identify periods when debris was deposited by icebergs at the site, related to calving activity of the glacier in these environments (Andresen et al., 2012).

4.1. Zone I, 13.4–11.2 ka cal BP – post-deglacial environment

The very base of the core (13.4–13.2 ka cal. BP) is characterised by coarse grains, a relatively high sedimentation rate and the presence of a large dropstone; possibly representing a diamicton. Above this, CT scans reveal distinct laminations, suggesting a proximal subglacial environment with a constant supply of material from the grounding zone (Ó Cofaigh and Dowdeswell, 2001, Fig. 6A) until 11.2 ka cal BP. This is supported by the relatively high sedimentation rate throughout this zone.

From the homogeneity of sediments and low abundance of benthic foraminifera, we infer that the site at 92G was free of grounded ice at least as early as 12.5 ka cal BP, corresponding to the oldest radiocarbon date used in the age model (486.5 cm) (Fig. 6A). Benthic foraminifera are present below this (from 13.1 ka cal BP), indicating marine conditions, but the amount of material was too small to date. As it was not possible to obtain material for dating below this, extrapolation of the age depth model indicates that deglaciation occurred before 12.5 ka cal BP and likely also before 13.4 ka cal BP, if accepting the more uncertain age model at the base of the core. Other studies have used morphological features to infer paleo-ice flow on the Northeast Greenland continental shelf; this implies that the grounded ice located at core site 92G was most likely the NEGIS, potentially flowing between the nearby islands or from a stream flowing south west, joined by the 79 N glacier (Arndt et al., 2015). The timing of the deglaciation and comparison with

other sites, is discussed in detail in Section 5.1.

The concentration of foraminifera, particularly calcareous species, from 13.1 ka cal BP period is low, suggesting an environment characterized by colder subsurface water conditions. This is supported by the relatively high assemblage percentages of *C. reniforme*, *Stainforthia* sp., *E. clavatum* and *G. oculus*, which infer a glaciomarine environment characterised by unstable conditions caused by turbid glacial meltwater and sea ice (Hald and Korsun, 1997; Jennings et al., 2020b; Polyak et al., 2002). *S. horvathi* is also abundant during this period; this species is an indicator of sea ice (Jennings et al., 2020b). On the other hand, the occurrence of *C. neoteretis* and *I. norcrossi* throughout this zone, suggest the presence of AW (Cage et al., 2021; Jennings et al., 2004; Jennings and Helgadottir, 1994; Seidenkrantz, 1995; Wollenburg et al., 2004). We hypothesise that AW may be entering as a subsurface current below the PW layer and sea ice, resulting in strong stratification. Relatively high, yet fluctuating, δS values in this zone suggest there were strong bottom water currents. Despite relatively high Ca/Fe, low foraminiferal concentrations suggest that the carbonate was transported from other regions and may be of terrestrial origin.

4.2. Zone II, 11.2–10.8 ka cal BP – brief ice shelf retreat

In this interval, sediments consist of a brownish silty clay and bioturbation, visible in the CT scans. The brief shift to bioturbated sediments suggests that the glacier retreated westwards (Fig. 6B). This is supported by an increase in IRD, inferred from high counts of grains over 3 mm, which has been linked to an increase in the marine calving rate of glaciers in fjords (Andresen et al., 2012; Mugford and Dowdeswell, 2010).

At the same time, the concentration of benthic foraminifera increases, also implying a brief retreat in the ice shelf and a transition towards open water conditions. The benthic foraminiferal assemblage is dominated by *C. neoteretis* and *I. norcrossi*, with slight increases in the latter; suggesting a continued presence, or slight increase, of AW at the site (Jennings et al., 2004; Jennings and Helgadottir, 1994; Knudsen et al., 2004; Wollenburg et al., 2004). This may have contributed to melting of icebergs and retreat of the NEGIS caused by increased calving rates (Mugford and Dowdeswell, 2010).

4.3. Zone III, 10.8–9.6 ka cal BP – return to proximal glacial environment

The sediment in this zone consists of distinct laminations. This suggests a brief return to proximal glaciomarine conditions (Fig. 6C). We propose this is caused by the settling of meltwater plumes from the nearby glacier, a theory supported by a slight increase in the sedimentation rate just after the start of this zone (Ó Cofaigh and Dowdeswell, 2001).

A study of the modern foraminiferal assemblages in the Petermann Fjord finds that *G. oculus* is most abundant near the ice shelf front (Jennings et al., 2020b). This supports the lithofacies interpretation that the site was overlain, or in close proximity to, the ice tongue of the NEGIS during this period. Furthermore, the overall concentration of foraminifera is low, suggesting a decline in productivity, which is typical of conditions beneath or in close proximity to an ice tongue. This has been related to a decline in meltwater discharge surface water productivity, which decreases the supply of nutrients and freshwater to bottom waters below (Waniek et al., 2005). A similar situation is recorded in the lithofacies of core PS100/270, located 130 km north of 92G (Fig. 1B), where laminated sediments are interpreted as proximal ice

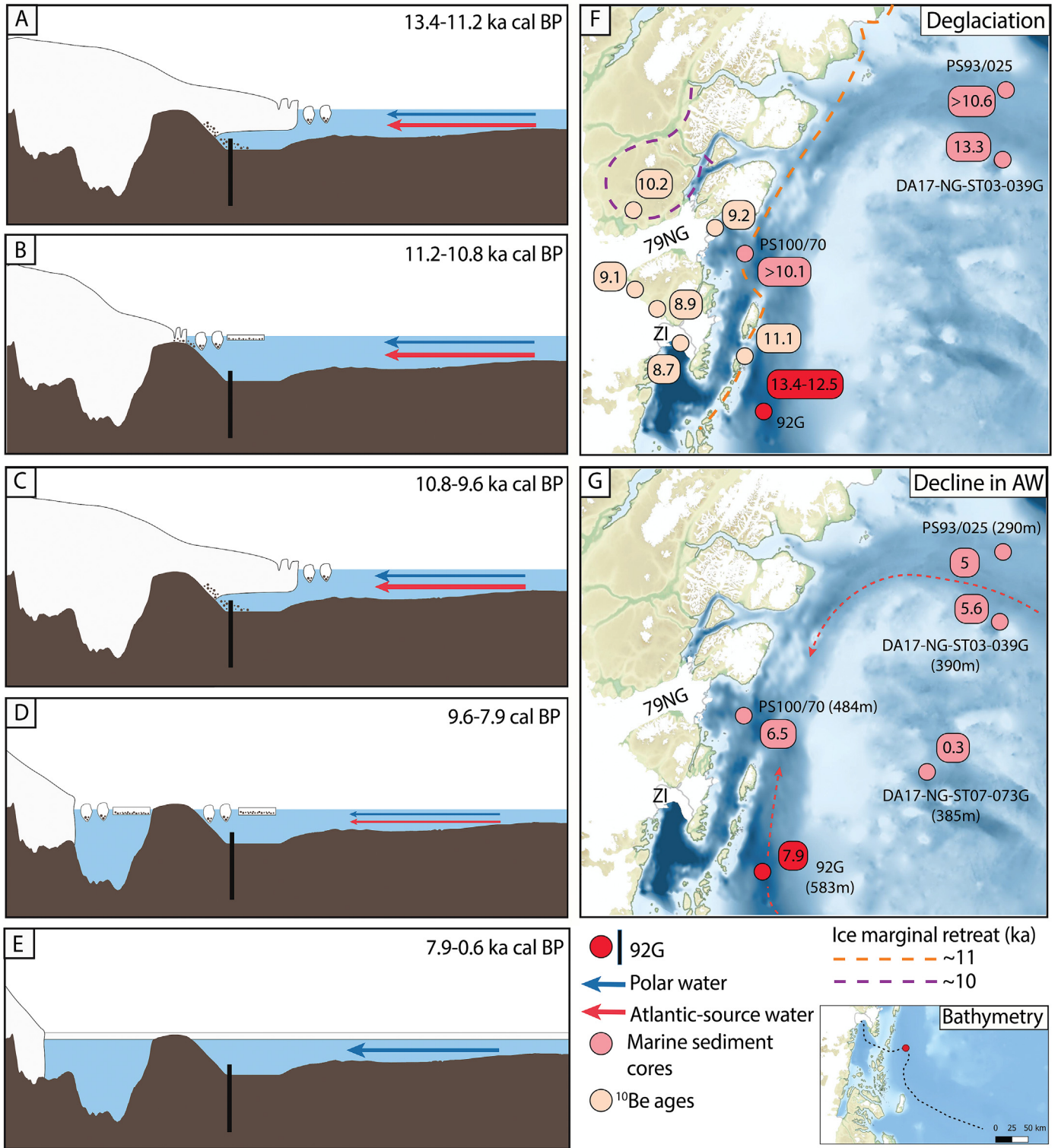


Fig. 6. A-E) The interaction between ocean circulation and NEGIS retreat and expansion on the Northeast Greenland continental shelf. The five time intervals represent the zones defined by the lithofacies and benthic foraminiferal data from core 92G. Coloured arrows represent the different water masses: Polar Water (PW), Atlantic Water (Return Atlantic Water and Arctic Atlantic Water). Larger arrows represent stronger currents and advection onto the shelf. The bathymetry is taken from Arndt et al., 2015, ice sheet height and grounding line position from 92G and Paleo-MIST 1.0 (Gowan et al., 2021) and sea level change from (Hjort, 1997). F) Timing of deglaciation on the Northeast Greenland continental shelf. Numbers represent timing in ka cal yrs BP. Marine sediment cores (pink) PS93/025 (Zehlich et al., 2020), DA17-NG-ST03-039G (Hansen et al., in review), PS100/70 (Syring et al., 2020a) and 92G (red) are used together with ¹⁰Be ages (Larsen et al., 2018). Lines for ice marginal retreat at 11 ka (orange) and 10 ka (purple) are taken from (Larsen et al., 2020), based on the same ¹⁰Be dates and ¹⁴C dates (Funder et al., 2011; Hjort, 1997; Nørgaard-Pedersen et al., 2008; Strunk et al., 2018). G) Timing of the decline in Atlantic source water is based on the same marine sediment cores as F) with the addition of DA17-NG-ST07-073G (Pados-Dibattista et al., 2022). Water depth for sediment cores are shown. Bathymetry of F and G is taken from Arndt et al., 2015; Yang et al., 2020. (For interpretation of the references to colour in this figure legend, the reader is referred to the Web version of this article.)

conditions between 10 and 9.6 ka cal BP (Syring et al., 2020a).

AW species still dominate the assemblage during this period; a study of modern assemblages found that *C. neoteretis* was found close to the ice tongue of the Petermann Glacier (Jennings et al., 2020b). This indicates that presence and advection of AW is still possible in close proximity to the ice tongue, perhaps the case in this instance. This period correlates with the onset of maximum Atlantic advection at subsurface and surface depths recorded in sediment cores from the eastern Fram Strait between 10.6 and 8.5 ka (Werner et al., 2016).

At the Petermann Fjord today, *E. clavatum* is excluded from ice tongue environments, despite its presence in other fjord areas (Jennings et al., 2020b). In 92G the abundance of *E. clavatum* is low during this period. We suggest that the site was situated close to the grounding line of the NEGIS, perhaps even under the ice tongue.

High-resolution biomarker data from Core PS93/025, located northeast of our study site in the Northeast-Water Polynya, show reduced-to-variable sea ice conditions between 10.2 and 9.3 ka with enhanced biological productivity. These conditions, together with the intensified inflow of AW, resulted in the elevated benthic and planktic foraminiferal concentrations at this site (Syring et al., 2020b).

4.4. Zone IV, 9.6–7.9 ka cal BP – retreat of the ice shelf

By 9.6 ka cal BP, an increase in bioturbation suggests a shift to a more distal glaciomarine environment as the NEGIS retreated westwards (Fig. 6D). In this environment, the sediment is mostly influenced by ocean conditions, rather than by the glacier itself. This aligns with Core PS100/270, which suggests a shift to a more distal proglacial environment after 9.6 ka cal BP (Syring et al., 2020a). The ice retreated to around 70 km behind its current position and halted between 7.8 and 1.2 ka cal BP (Syring et al., 2020a); this has been attributed to warming atmospheric and oceanic temperatures (Arndt et al., 2015, 2017; Evans et al., 2009; Tabone et al., 2019; Winkelmann et al., 2010).

Similarly, there is an increase of some productivity-indicator foraminifera species (*V. arctica*/*N. fragilis*) and overall foraminiferal concentration in this zone, which would suggest a shift towards warmer conditions, with an increase in nutrient supply. The regional supply of freshwater from basal melting of the tongue and grounding line of the NEGIS (Bamber et al., 2012) may have triggered this (Cape et al., 2019; Syring et al., 2020a). This aligns with the timing of onset of the Holocene Thermal Maximum (dated 9.5–7 ka cal BP) from ice core records (e.g. Johnsen et al., 2001; Vinther et al., 2009), when sea ice free conditions prevailed (Funder et al., 2011) and marine terminating glaciers retreated (Nørgaard-Pedersen et al., 2008). In the Western Fram Strait, foraminiferal faunas and stable isotope data, combined with Ca/Fe ratios, indicate that there was a maximum biological productivity between 10.6 and 8 ka cal BP; this is hypothesised to be caused by the strong advection of AW, via the Return Atlantic Current, across the Fram Strait (Zehlich et al., 2020). Biomarker data from the same core suggests reduced ice cover which would have allowed foraminifera species to thrive (Zehlich et al., 2020). This suggests that the warm water signal may have travelled along the Norske Trough to our site at this time. Reconstructions of seawater temperatures in the Nordic Seas and Barents Sea suggest that this could be driven by temperature increases there (Risembroakken et al., 2011).

The gradual increase in *E. clavatum*, from 8.5 ka cal BP, is interpreted as an onset of a fresher unstable period, linked to a stronger advection of polar East Greenland Current waters or the retreating glacier, as suggested close to the front of 79NG (Syring et al., 2020a). Minimum IRD were also found in this time interval (9.6–7.5 ka cal BP) in Core PS100/270 (Syring et al., 2020a) and PS2623 (Stein,

2008), indicating cold, fresh waters.

The continued dominance of AW species suggest the presence and influence of subsurface AW beneath the PW at the core site until 7.9 ka cal BP. Other sites also record continued AW advection across the Northeast Greenland continental shelf until 8 ka cal BP, but with a continued presence beyond this period (Syring et al., 2020a; Zehlich et al., 2020).

4.5. Zone V 7.9–0.6 ka cal BP – decline in Atlantic Water flow

The start of this zone is characterised by a sharp decline in benthic foraminiferal concentrations, most noticeably in the AW species, and a decline in sedimentation rate. Concurrently, the species *E. clavatum* increases before fully disappearing and the foraminiferal assemblage becomes dominated by agglutinated species. We propose that this shift signifies that the influx of AW became severely reduced or fully ceased at this time, and that PW reached the seafloor beneath perennial sea ice after 7.9 ka cal BP (Fig. 6E). Stratification and favourable conditions for the formation of sea ice would reduce bottom water ventilation and create corrosive waters (Lloyd et al., 2007); potentially contributing to the dissolution of calcareous foraminifera. However, the disappearance of calcareous species could also be linked to a change in the sedimentation rate as suggested in studies from other near-glacier environments (Aksu, 1983; Lloyd et al., 2007). In 92G, the lower part of the core is characterised by a higher sedimentation rate and presence of calcareous foraminifera. In contrast, in the uppermost 60 cm the sedimentation rate is low with no or very few calcareous foraminifera present. Whilst this may partially explain this pattern, the sedimentation rate begins to decline before the percentage calcareous foraminifera do, suggesting that the other mechanisms aforementioned are likely the dominant driver of this change. The reduced sediment accumulation rates may be linked to increased sea ice cover and reduced melting of the NEGIS as a consequence of the colder water. The decline in AW is discussed in more detail in Section 5.2.

At the onset of Zone V, *M. barleeanus*, a eutrophic species, is present in its highest abundance of the entire record; this species is often found in areas with high buried organic material (Polyak et al., 2002; Caralp, 1989). Similarly, the presence of *A. weddellensis* and *E. takayanagii* in one sample at the start of this zone suggests that a high marine productivity characterised the area here (Fentimen et al., 2020; Lamshead and Gooday, 1990). We infer that before the full onset of perennial sea ice, the sea ice margin rested in the vicinity of our site for some time (Syring et al., 2020a). However, the low foraminiferal concentrations are much lower than in the sub-ice-shelf phase, suggesting there was not a productivity peak amongst all species. *P. bipolaris* also increases rapidly from the start of this zone, peaking at 4 ka cal BP; this species suggest the influence of PW (Lloyd, 2006), and has been found under polar waters in the Canadian Arctic (Vilks, 1989) and fjords in eastern Greenland (Jennings and Helgadottir, 1994). This is supported by the presence of *Reophax* sp. during this period; this species is found in the fjords of eastern Baffin Bay and in cold, low salinity waters (Vilks, 1969).

The return and peaks of calcareous foraminifera, including *C. neoteretis* and *I. norcrossi*, at 2.5 ka cal BP and 0.6 ka cal BP implies a return of AW. The low sedimentation rate and maintained dominance of agglutinated species suggests perennial sea ice was still overlaying the site. There is also a short peak in *A. glomerata*, which is common on continental shelves at high latitudes and is linked to AW, further supporting the inference that there may have still been some influence from these waters in this section of the core (Hald and Korsun, 1997; Lloyd, 2006).

5. Discussion

The discussion focuses on the two main changes observed in this study: 1) the deglaciation (start of Zone I) and 2) the dramatic decline in AW inflow (Zone V).

5.1. Late weichselian initial deglaciation of the northeast Greenland continental shelf (>13.4 ka cal BP)

Results from 92G suggest that retreat of grounded ice occurred prior to 12.5 ka cal BP, and probably before 13.4 ka cal BP, depending on the extrapolated age in the bottom of our age-depth model. Radiocarbon dates collected from the Northeast Greenland coastline close to the present NEGIS suggest that deglaciation of this area occurred prior to 9.7 ka cal BP (Bennike and Björck, 2002). ^{10}Be records often yield significantly older estimates than radiocarbon ages and arguably provide a better record of ice retreat (Larsen et al., 2020). A combination of ^{14}C and ^{10}Be ages suggest that the outer coast of the Northeast Greenland continental shelf was deglaciated by 11.7 ± 4 ka cal BP (Larsen et al., 2018). This aligns with results from marine deposits in NE Kronprins Christian Land, which indicate an ice-free coast by 11.1 ka cal BP (converted from ^{14}C age reported by Hjort, 1997). Homogeneous sediments from a marine sediment core collected in the western Fram Strait suggest retreat of grounded ice past the site at 10.6 ka cal BP, defined as a minimum age for deglaciation, aligning with the slightly later retreat recorded on the continental shelf itself (Zehnich et al., 2020). However, results from marine sediment core DA17-NG-ST03-039G (Fig. 6F), located northeast of 92G in the Fram Strait, record onset of deglacial conditions prior to 13.3 ka cal BP (Hansen et al., in review). This is compatible with the earlier deglacial onset recorded at our site, given its more north-easterly positioning.

However, two sites located relatively close to 92G suggest a later deglacial onset (Fig. 6F). ^{10}Be dates from Bourbon Øer, located west of core site 92G, indicate deglaciation at 11.1 ka cal BP (Larsen et al., 2018). The lowest unit of sediment of Core PS100/270, located approximately 130 km north of 92G, is characterised by a stiff, over-consolidated diamicton, interpreted as a subglacial environment, with the transition to certain marine conditions at least as early as 10.1 ka (Syring et al., 2020a). The earlier retreat of ice at our site may be a reflection of its more distal location to the coastline than the core and ^{10}Be dates aforementioned, where, after an initial retreat from our site, the ice may have come to a rest on the Bourbon Øer and near Core PS100/270 for a couple of millennia.

The presence of AW at the core site directly after the deglaciation suggests that it may have played a role in the retreat of ice in Northeast Greenland; this pattern is seen elsewhere (e.g. Syring et al., 2020a; Hansen et al., in review). Together with orbital forcing of higher summer temperatures (Berger and Loutre, 1991) and a thinner Arctic halocline (Jakobsson et al., 2010), the presence of AW in Hall Basin, Nares Strait, during the deglaciation provides further evidence that it may have assisted in ice retreat (Jennings et al., 2011).

5.2. Decline in Atlantic Water flow after 7.9 ka cal BP

During the deglacial and Early Holocene, the Northeast Greenland continental shelf was characterised by a significant influx of AW; this may have played a role in its seemingly early deglaciation. However, data from 92G imply at ca. 7.9 ka cal yr BP the inner Northeast Greenland continental shelf experienced a major change in oceanographic conditions, covered in Zone V. The decline in the sedimentation rate, in overall benthic foraminiferal concentrations, and in particular the shift from an assemblage dominated by AW calcareous species to agglutinated species

suggest that there was change in the subsurface waters carried by the East Greenland Current; specifically a reduction in AW and increase in PW beneath perennial sea ice. A drop in the sedimentation rate is recorded in core PS100/270 at 7.5 ka cal BP, just north of 92G (Syring et al., 2020a). This is also seen on the southern NE Greenland shelf off Young Sound, where sedimentation rates dropped from 8.7 ka BP and again further at from 7.5 ka cal BP (Jackson et al., in review), suggesting a region-wide pattern of reduced sediment flux from land after the Early Holocene.

Throughout the Arctic and larger North Atlantic region, records reveal a pattern of Early to Mid Holocene warm conditions influenced by AW, followed by cooling during the Mid to Late Holocene (e.g. Koç et al., 1993; Nesje and Dahl, 1993; Syring et al., 2020a; Williams et al., 1995; Zehnich et al., 2020). The Mid to Late Holocene is defined by minimum solar insolation, a southward shift of the polar front, and a strengthening of the East Greenland Current (Bauch et al., 2001; Laskar et al., 2004; Müller et al., 2012; Ran et al., 2006). Results from sediment cores in the Nordic Seas suggest a widespread gradual cooling in summer surface waters from 7 ka cal BP (Andersen et al., 2004; Koç et al., 1993). This resulted in a reduction in heat transported northwards via the NAC and West Spitsbergen Current towards the Arctic Ocean and the western and northern Svalbard shelf (Consolaro et al., 2018; Ślubowska-Woldengen et al., 2007).

A cooling trend is also recorded from 6 ka in two sediment cores from the eastern Fram Strait (Werner et al., 2016). Similarly, in the Nansen Trough on the East Greenland shelf, benthic foraminifera, stable isotopes and IRD fluxes indicate a shift towards polar conditions at 5 ka (Jennings et al., 2002). This pattern is also visible on the Northeast Greenland continental shelf; yet the timing of the onset of the decline in AW differs between sites (Fig. 7G).

Sortable silt values, planktic foraminifera, and stable isotope data of planktic and benthic foraminifera from Core P293/25, on the outer Northeast Greenland continental shelf, indicate a strong westward advection of AW until about 8 ka cal BP, when productivity weakened and sea ice cover expanded (Zehnich et al., 2020). However, AW is present until 5 ka cal BP. Results from the nearby located core DA17-NG-ST03-073G suggest AW prevailed until 5.6 ka cal BP (Hansen et al., in review). This aligns with the isostatic rebound of the Northeast Greenland shelf; around 50 m between 8 and 4 ka cal BP (Hjort, 1997), which may have lifted the sea floor of the continental shelf to those depths more influenced by PW (Zehnich et al., 2020).

On the central Northeast Greenland shelf, cooling of the subsurface water started ca. 6.2 ka cal BP, with further cooling at 4.2 and 3.2 ka cal BP (Pados-Dibattista et al., 2022). On the inner shelf, close to the 79 N glacier, the abundance of *C. neoteretis* remains high until 6.5 ka cal BP (Syring et al., 2020a). However, the flux of AW species at the latter site follows a similar pattern to 92G, with a decline at 8.2 ka cal BP; yet the presence of AW species suggests the continued presence of AW until the late Holocene (Fig. 7; Syring et al., 2020a).

In order to explain the discrepancies in the timing of AW presence and advection between core sites on the Northeast Greenland continental shelf, we examine the potential transport pathways of AW towards the study sites, specifically the Norske and Westwind troughs. The main sources of AW in the Norske and Westwind troughs are Return Atlantic Water and Arctic Atlantic Water, respectively (Rudels et al., 2012; Schaffer et al., 2017). Whilst few hydrographic measurements exist in the region between the calving front of the 79NG and the trough system, CTD profiles show AW is present in front of 79NG and in the cavity below (Schaffer et al., 2017). It is believed that the Norske Trough plays the pivotal role in transporting AW towards 79NG (Schaffer et al., 2017). Wilson and Straneo (2015) show that warm water from the

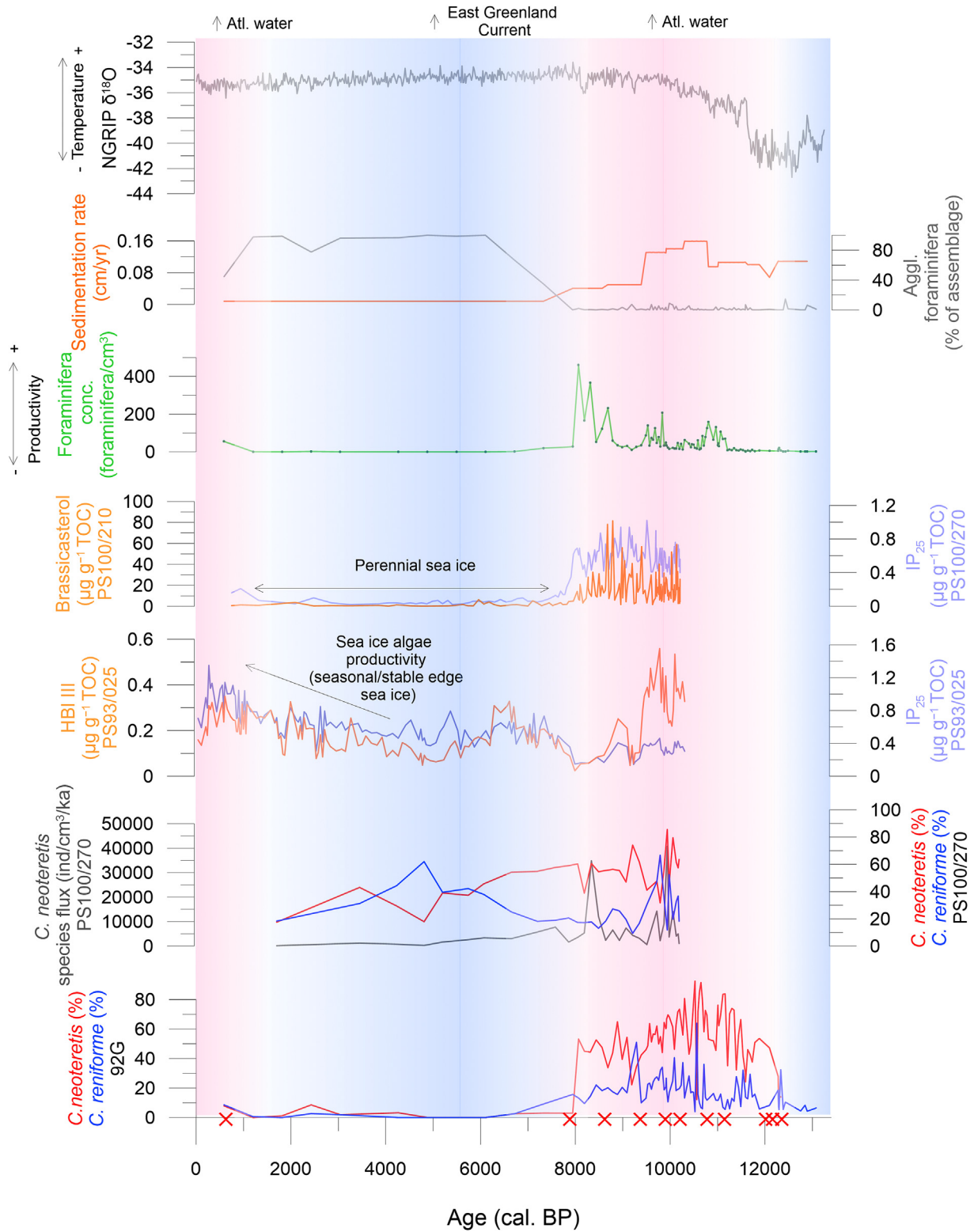


Fig. 7. Summary figure depicting data from numerous sources spanning the Holocene. The NGRIP $\delta^{18}\text{O}$ dataset (NGRIP-Members, 2004) is plotted alongside the sedimentation rate, foraminifera concentration (resolution of data shown in dark green), agglutinated foraminifera percentage, abundance of species *C. neoteretis* and *C. reniforme* from 92G. Radiocarbon dates are plotted (red crosses). Biomarker data from PS93/025 (Syring et al., 2020b) and PS100/270, together with *C. neoteretis* (flux and %) and *C. reniforme* (%) (Syring et al., 2020a) are also plotted. (For interpretation of the references to colour in this figure legend, the reader is referred to the Web version of this article.)

Westwind Trough cannot enter close to 79NG through the northern inlet (Dijmphna Sund), as previously proposed (Mayer et al., 2000) due to a 170 m sill. However, Schaffer et al. (2017) indicate that Westwind Trough possibly still plays a minor role in transporting AW towards 79NG today. As sea levels were higher in the Early Holocene, due to isostatic depression, this may have allowed AW to reach PS100/270 from the Westwind Trough (Hjort, 1997; Strunk et al., 2018). However, it is likely that the transport pathway of AW has predominantly been the Norske Trough for cores sites PS100/270 and 92G, with minor contributions from the Westwind Trough. If the Norske Trough is the primary pathway for AW towards sites 92G and PS100/270, differences in the onset of the decline in AW cannot be explained by transport pathways alone.

The cause behind the discrepancies in the timing of AW at 92G, PS100/270, and PS93/025 perhaps lies in the local environment, specifically the water depth at which the cores were retrieved. The water depth at PS100/270 and PS93/025 is shallower (484 m and 290 m, respectively) than at 92G (583 m) (Fig. 6G). This means that after 7.9 ka cal. BP the basin in which 92G is located was likely dominated by deeper, colder water, originating from the East Greenland Current, earlier than PS100/270 and PS93/025. We argue that this is the most likely cause of the discrepancies in timing, yet further analysis of the foraminiferal assemblages and local environment in the region is required to ascertain this.

A decline in biomarker concentrations (IP₂₅, HBI III, brassicasterol and dinosterol) at 7.5 ka cal BP in Core PS100/270 suggests nearly permanent sea ice cover close to 79NG, with some summer ice thinning, until 0.7 ka cal BP (Fig. 7; Syring et al., 2020a). This supports findings from 92G, which suggests perennial sea ice overlaid the site from 7.9 ka cal BP. Further east on the Northeast Greenland continental shelf, biomarker data suggests a continued presence of seasonal sea ice from 7.9 to 4.9 ka cal BP (Syring et al., 2020b) with low overall foraminiferal abundance and CaCO₃ suggesting low productivity (Fig. 7; Zehnick et al., 2020). This aligns with an increase in abundance of Arctic diatoms between 6.8 and 5.6 ka cal BP on the North Icelandic shelf (Ran et al., 2006). Together, this implies a strengthening of the East Greenland Current, which would have carried drift ice from the Arctic southwards (Andrews et al., 2009; Cabedo-Sanz et al., 2016).

The final part of our record is characterised by peaks in calcareous species and the overall foraminiferal concentration, but with a maintained presence of agglutinated species. This suggests a potential shift towards seasonal sea ice or open water conditions with presence of AW in the uppermost part of the record, similar to those observed in the region today. However, there is uncertainty surrounding the exact timing due to the lack of radiocarbon dates in the uppermost part of the core; the shift may have occurred earlier or later due to uncertainty in the age model.

6. Conclusion

The presented multiproxy dataset, comprising foraminifera, geochemical, and sedimentological analysis of Gravity Core 92G documents changes to ocean circulation and deglacial retreat of the NEGIS on the Northeast Greenland continental shelf throughout the Holocene:

1. The site experienced marine conditions throughout, which according to our age model covers the last 13.4 ka cal BP, albeit with the lowermost certain ¹⁴C date at 12.5 ka cal BP. The timing of deglaciation is thus certain to have occurred before 12.5 ka cal BP and likely before 13.4 ka cal BP, assuming a constant sedimentation rate.
2. Between 13.4 and 11.2 ka cal BP, laminated sediments and foraminifera commonly found under floating ice sheets or

perennial sea ice shows that the environment was characterized by the close proximity to the NEGIS with an ice shelf extending across the site. At subsurface levels, the persistent and strong influx of AW may have impacted the speed of the ice retreat.

3. A short interval (11.2–10.8 ka cal BP) with a reduced sedimentation rate, shift from laminated to bioturbated sediments, and presence of IRD, documents the retreat of the ice shelf and a shift to open water conditions.
4. The period 10.8–9.6 ka cal BP saw a renewal of glacier-proximal conditions, dominated by colder subsurface water conditions, but influx of AW persisted. The ice shelf may again have extended across our study site.
5. From 9.6 to 7.9 ka cal BP, the NEGIS retreated westwards. There is evidence of an influx of PW at the surface, with the continued presence of AW beneath it.
6. A drastic shift in the ocean circulation occurred at ca. 7.9 ka cal BP. A sharp decline in AW at the site corresponds to an increase in PW influx, flowing beneath perennial sea ice. There is once more a shift to seasonal or open water conditions from 0.6 ka cal BP.

Author contributions

Joanna Davies: Conceptualization, Formal Analysis, Writing - Original Draft, Writing - Review & Editing; Visualization, Project Management.; **Anders Møller Mathiasen:** Formal Analysis.; **Kristiane Kristiansen:** Formal Analysis.; **Katrine Elnegaard Hansen:** Analysis, Review & Editing.; **Lukas Wacker:** Formal Analysis, Review & Editing.; **Aage Kristian Olsen Alstrup:** Formal Analysis.; **Ole Lajord Munk:** Analysis.; **Christof Pearce:** Supervision, Resources, Conceptualization, Visualization, Data Curation, Writing - Review & Editing.; **Marit-Solveig Seidenkrantz:** Supervision, Funding acquisition, Resources, Conceptualization, Cruise planning and Leading, Data Curation, Writing - Review & Editing.

Financial support

The NorthGreen2017 expedition was funded by the Danish Centre for Marine Research and the Natural Science and Engineering Research Council of Canada. The research was funded by the Danish Council for Independent Research (grants no. 7014-00113 B (G-Ice)) and 0135-00165 B ((GreenShelf) to MSS), and by the iClimate Centre of Aarhus University, with additional funding from the European Union's Horizon 2020 research and innovation program under Grant Agreement No. 869383 (ECOTIP).

Data availability

Data for this research is available on PANGAEA.

Declaration of competing interest

The authors declare that they have no known competing financial interests or personal relationships that could have appeared to influence the work reported in this paper.

Acknowledgements

We would like to extend our warmest thanks to the crew, captain and scientists onboard the NorthGreen2017 exhibition with *RV Dana*. We would also like to thank Trine Ravn-Jensen for running and composing the XRF dataset and Teodóra Pados-Dibattista for assistance with foraminiferal picking and identification for radiocarbon dating. We thank Jørgen Bendtsen, ClimateLab, who

undertook the CTD measurements. We thank Anne de Vernal, who acquired part of the funding for the cruise. We also thank the editor and two un-named reviewers for their valuable comments.

Appendix A. Supplementary data

Supplementary data to this article can be found online at <https://doi.org/10.1016/j.quascirev.2022.107530>.

References

- Aagaard, K., Coachman, L.K., 1968. The East Greenland current north of Denmark Strait: Part I. *Arctic* 21, 181–200.
- Aksu, A.E., 1983. Holocene and pleistocene dissolution cycles in deep-sea cores of Baffin Bay and Davis Strait: palaeoceanographic implications. *Mar. Geol.* 53, 331–348. [https://doi.org/10.1016/0025-3227\(83\)90049-X](https://doi.org/10.1016/0025-3227(83)90049-X).
- Amundson, J.M., Fahnestock, M., Truffer, M., Brown, J., Lüthi, M.P., Motyka, R.J., 2010. Ice mélange dynamics and implications for terminus stability, Jakobshavn Isbræ, Greenland. *J. Geophys. Res. Earth Surf.* 115. <https://doi.org/10.1029/2009JF001405>.
- An, L., Rignot, E., Wood, M., Willis, J.K., Mouginot, J., Khan, S.A., 2021. Ocean melting of the Zachariae Isstrøm and Nioghalvfjerdingsfjorden glaciers, northeast Greenland. *Proc. Natl. Acad. Sci. Unit. States Am.* 118, e2015483118. <https://doi.org/10.1073/pnas.2015483118>.
- Andersen, C., Koç, N., Jennings, A., Andrews, J.T., 2004. Nonuniform response of the major surface currents in the Nordic Seas to insolation forcing: implications for the Holocene climate variability. *Paleoceanography* 19. <https://doi.org/10.1029/2002PA000873>.
- Andresen, C.S., Straneo, F., Ribergaard, M.H., Bjørk, A.A., Andersen, T.J., Kuijpers, A., Nørgaard-Pedersen, N., Kjær, K.H., Schjøth, F., Weckström, K., Ahlstrøm, A.P., 2012. Rapid response of Helheim Glacier in Greenland to climate variability over the past century. *Nat. Geosci.* 5, 37–41. <https://doi.org/10.1038/ngeo1349>.
- Andrews, J.T., Darby, D., Eberle, D., Jennings, A.E., Moros, M., Ogilvie, A., 2009. A robust, multisite Holocene history of drift ice off northern Iceland: implications for North Atlantic climate. *Holocene* 19, 71–77. <https://doi.org/10.1177/0959683608098953>.
- Arndt, J.E., Jokat, W., Dorschel, B., Myklebust, R., Dowdeswell, J.A., Evans, J., 2015. A new bathymetry of the Northeast Greenland continental shelf: constraints on glacial and other processes. *G-cubed* 16, 3733–3753. <https://doi.org/10.1002/2015GC005931>.
- Arndt, J.E., Jokat, W., Dorschel, B., 2017. The last glaciation and deglaciation of the Northeast Greenland continental shelf revealed by hydro-acoustic data. *Quat. Sci. Rev.* 160, 45–56. <https://doi.org/10.1016/j.quascirev.2017.01.018>.
- Axford, Y., Losee, S., Briner, J.P., Francis, D.R., Langdon, P.G., Walker, I.R., 2013. Holocene temperature history at the western Greenland Ice Sheet margin reconstructed from lake sediments. *Quat. Sci. Rev.* 59, 87–100. <https://doi.org/10.1016/j.quascirev.2012.10.024>.
- Bamber, J., Van Den Broeke, M., Ettema, J., Lenaerts, J., Rignot, E., 2012. Recent large increases in freshwater fluxes from Greenland into the North Atlantic. *Geophysical Research Letters* 39 (19). <https://doi.org/10.1029/2012GL052552>.
- Bard, E., Tuna, T., Fagault, Y., Bonvalot, L., Wacker, L., Fahrni, S., Sval, H.-A., 2015. AixMICADAS, the accelerator mass spectrometer dedicated to 14C recently installed in Aix-en-Provence, France. *Nucl. Instrum. Methods Phys. Res. Sect. B Beam Interact. Mater. At. The Thirteenth Accelerator Mass Spectrometry Conference* 361, 80–86. <https://doi.org/10.1016/j.nimb.2015.01.075>.
- Batchelor, C.L., Dowdeswell, J.A., 2014. The physiography of High Arctic cross-shelf troughs. *Quat. Sci. Rev.* APEX II: Arctic Palaeoclimate and its Extremes 92, 68–96. <https://doi.org/10.1016/j.quascirev.2013.05.025>.
- Bauch, H.A., Erlenkeuser, H., Spielhagen, R.F., Struck, U., Matthiessen, J., Thiede, J., Heinemeier, J., 2001. A multiproxy reconstruction of the evolution of deep and surface waters in the subarctic Nordic seas over the last 30,000yr. *Quat. Sci. Rev.* 20, 659–678. [https://doi.org/10.1016/S0277-3791\(00\)00098-6](https://doi.org/10.1016/S0277-3791(00)00098-6).
- Bennike, O., Björck, S., 2002. Chronology of the last recession of the Greenland ice sheet. *J. Quat. Sci.* 17, 211–219. <https://doi.org/10.1002/jqs.670>.
- Berger, A., Loutre, M.F., 1991. Insolation values for the climate of the last 10 million years. *Quat. Sci. Rev.* 10, 297–317. [https://doi.org/10.1016/0277-3791\(91\)90033-Q](https://doi.org/10.1016/0277-3791(91)90033-Q).
- Budéus, G., Schneider, W., Kattner, G., 1997. Distribution and exchange of water masses in the Northeast Water polynya (Greenland Sea). *J. Mar. Syst.* 10, 123–138. [https://doi.org/10.1016/S0924-7963\(96\)00074-7](https://doi.org/10.1016/S0924-7963(96)00074-7).
- Cabedo-Sanz, P., Belt, S.T., Jennings, A.E., Andrews, J.T., Geirsdóttir, Á., 2016. Variability in drift ice export from the Arctic Ocean to the North Icelandic Shelf over the last 8000 years: a multi-proxy evaluation. *Quat. Sci. Rev.* 146, 99–115. <https://doi.org/10.1016/j.quascirev.2016.06.012>.
- Cage, A.G., Pienkowski, A.J., Jennings, A., Knudsen, K.L., Seidenkrantz, M.-S., 2021. Comparative analysis of six common foraminiferal species of the genera *Cassidulina*, *Paracassidulina*, and *Islandiella* from the Arctic–North Atlantic domain. *J. Micropalaeontol.* 40, 37–60. <https://doi.org/10.5194/jm-40-37-2021>.
- Cape, M.R., Straneo, F., Beaird, N., Bundy, R.M., Charette, M.A., 2019. Nutrient release to oceans from buoyancy-driven upwelling at Greenland tidewater glaciers. *Nature Geoscience* 12 (1), 34–39.
- Caralp, M.H., 1989. Abundance of *Bulimina exilis* and *Melonis barleeianum*: Relationship to the quality of marine organic matter. *Geo-Marine Letters* 9 (1), 37–43. <https://doi.org/10.1007/BF02262816>.
- Consolaro, C., Rasmussen, T.L., Panieri, G., 2018. Palaeoceanographic and environmental changes in the eastern Fram Strait during the last 14,000 years based on benthic and planktonic foraminifera. *Mar. Micropaleontol.* 139, 84–101. <https://doi.org/10.1016/j.marmicro.2017.11.001>.
- Cowton, T.R., Sole, A.J., Nienow, P.W., Slater, D.A., Christoffersen, P., 2018. Linear response of east Greenland's tidewater glaciers to ocean/atmosphere warming. *Proc. Natl. Acad. Sci. Unit. States Am.* 115, 7907–7912. <https://doi.org/10.1073/pnas.1801769115>.
- de Steur, L., Hansen, E., Mauritzen, C., Beszczynska-Moeller, A., Fahrbach, E., 2014. Impact of recirculation on the east Greenland current in Fram Strait: results from moored current meter measurements between 1997 and 2009. *Deep-Sea Res. Part A Oceanogr. Res. Pap.* 92. <https://doi.org/10.1016/j.dsr.2014.05.018>.
- El bani Altuna, N., Rasmussen, T.L., Ezat, M.M., Vadakkepulyambatta, S., Groeneveld, J., Greaves, M., 2021. Deglacial bottom water warming intensified Arctic methane seepage in the NW Barents Sea. *Communications Earth & Environment* 2 (1), 1–9.
- Enderlin, E.M., Howat, I.M., Jeong, S., Noh, M.-J., van Angelen, J.H., van den Broeke, M.R., 2014. An improved mass budget for the Greenland ice sheet. *Geophys. Res. Lett.* 41, 866–872. <https://doi.org/10.1002/2013GL059010>.
- Evans, J., Cofaigh, C.O., Dowdeswell, J.A., Wadhams, P., 2009. Marine geophysical evidence for former expansion and flow of the Greenland Ice Sheet across the north-east Greenland continental shelf. *J. Quat. Sci.* 24, 279–293. <https://doi.org/10.1002/jqs.1231>.
- Farmer, J.R., Sigman, D.M., Granger, J., Underwood, O.M., Fripiat, F., Cronin, T.M., Martínez-García, A., Haug, G.H., 2021. Arctic Ocean stratification set by sea level and freshwater inputs since the last ice age. *Nat. Geosci.* 14 (9), 684–689.
- Fentimen, R., Lim, A., Rüggeberg, A., Wheeler, A.J., Van Rooij, D., Foubert, A., 2020. Impact of bottom water currents on benthic foraminiferal assemblages in a cold-water coral environment: the Moira Mounds (NE Atlantic). *Mar. Micropaleontol.* 154, 101799. <https://doi.org/10.1016/j.marmicro.2019.101799>.
- Fréchette, B., de Vernal, A., 2009. Relationship between Holocene climate variations over southern Greenland and eastern Baffin Island and synoptic circulation pattern. *Clim. Past* 5, 347–359. <https://doi.org/10.5194/cp-5-347-2009>.
- Funder, S., 1982. 14C-dating of samples collected during the 1979 expedition to North Greenland. *Rapp. - Grnl. Geol. Undersøgelse* 110, 9–14.
- Funder, S., 1990. *Late Quaternary Stratigraphy and Glaciology in the Thule Area, Northwest Greenland*. Museum Tusulanum Press.
- Funder, S., Kjeldsen, K.K., Kjær, K.H., Ó Cofaigh, C., 2011. Chapter 50 - the Greenland ice sheet during the past 300,000 years: a review. In: Ehlers, J., Gibbard, P.L., Hughes, P.D. (Eds.), *Developments in Quaternary Sciences, Quaternary Glaciations - Extent and Chronology*. Elsevier, pp. 699–713. <https://doi.org/10.1016/B978-0-444-53447-7.00050-7>.
- Gowan, E.J., Zhang, X., Khosravi, S., Rovere, A., Stocchi, P., Hughes, A.L.C., Gyllencreutz, R., Mangerud, J., Svendsen, J.-I., Lohmann, G., 2021. A new global ice sheet reconstruction for the past 80,000 years. *Nat. Commun.* 12, 1199. <https://doi.org/10.1038/s41467-021-21469-w>.
- Grobe, H., 1987. A simple method for the determination of ice-rafted debris in sediment cores. *Polarforschung* 57, 123–126.
- Håkansson, S., 1973. University of Lund radiocarbon dates VI. *Radiocarbon* 15 (3), 493–513.
- Hald, M., Korsun, S., 1997. Distribution of modern benthic foraminifera from fjords of Svalbard, European Arctic. *J. Foraminifer. Res.* 27, 101–122. <https://doi.org/10.2113/gsjfr.27.2.101>.
- Hansen, K.E., Lorenzen, J., Davies, J., Wacker, L., Pearce, C., Seidenkrantz, M.-S., submitted. Deglacial to Mid Holocene Environmental Conditions on the Northeastern Greenland Shelf, Western Fram Strait.
- Hass, H.C., 2002. A method to reduce the influence of ice-rafted debris on a grain size record from northern Fram Strait, Arctic Ocean. *Polar Res.* 21, 299–306. <https://doi.org/10.1111/j.1751-8369.2002.tb00084.x>.
- Heaton, T.J., Köhler, P., Butzin, M., Bard, E., Reimer, R.W., Austin, W.E., Ramsey, C.B., Grootes, P.M., Hughen, K.A., Kromer, B., Reimer, P.J., 2020. Marine20—the marine radiocarbon age calibration curve (0–55,000 cal BP). *Radiocarbon* 62 (4), 779–820.
- Helm, V., Humbert, A., Miller, H., 2014. Elevation and elevation change of Greenland and Antarctica derived from CryoSat-2. *Cryosphere* 8, 1539–1559. <https://doi.org/10.5194/tc-8-1539-2014>.
- Hjort, C., 1997. Glaciation, climate history, changing marine levels and the evolution of the Northeast Water polynya. *J. Mar. Syst.* 10, 23–33. [https://doi.org/10.1016/S0924-7963\(96\)00068-1](https://doi.org/10.1016/S0924-7963(96)00068-1).
- Holland, D.M., Thomas, R.H., de Young, B., Ribergaard, M.H., Lyberth, B., 2008. Acceleration of Jakobshavn Isbræ triggered by warm subsurface ocean waters. *Nat. Geosci.* 1, 659–664. <https://doi.org/10.1038/ngeo316>.
- Hopkins, T.S., 1991. The GIN Sea—a synthesis of its physical oceanography and literature review 1972–1985. *Earth Sci. Rev.* 30, 175–318. [https://doi.org/10.1016/0012-8252\(91\)90001-V](https://doi.org/10.1016/0012-8252(91)90001-V).
- Hughes, A.L.C., Rainsley, E., Murray, T., Fogwill, C.J., Schnabel, C., Xu, S., 2012. Rapid response of Helheim Glacier, southeast Greenland, to early Holocene climate warming. *Geology* 40, 427–430. <https://doi.org/10.1130/G32730.1>.
- Jackson, R., Andreasen, N., Oksman, M., Andersen, T.J., Christof Pearce, C., Seidenkrantz, M.-S., Ribeiro, S. Marine conditions and development of the sirius water polynya on the north-east Greenland shelf during the younger dryas-holocene. *Quat. Sci. Rev.*, in review.

- Jakobsson, M., Nilsson, J., O'Regan, M., Backman, J., Löwemark, L., Dowdeswell, J.A., Mayer, L., Polyak, L., Colleon, F., Anderson, L.G., Björk, G., Darby, D., Eriksson, B., Hanslik, D., Hell, B., Marcussen, C., Sellén, E., Wallin, A., 2010. An Arctic Ocean ice shelf during MIS 6 constrained by new geophysical and geological data. *Quat. Sci. Rev.*, APEX: Arctic Palaeoclimate and its Extremes 29, 3505–3517. <https://doi.org/10.1016/j.quascirev.2010.03.015>.
- Jennings, A.E., Helgadottir, G., 1994. Foraminiferal assemblages from the fjords and shelf of eastern Greenland. *J. Foraminif. Res.* 24, 123–144. <https://doi.org/10.2113/gsjfr.24.2.123>.
- Jennings, A.E., Knudsen, K.L., Hald, M., Hansen, C.V., Andrews, J.T., 2002. A mid-Holocene shift in Arctic sea-ice variability on the East Greenland Shelf. *Holocene* 12, 49–58. <https://doi.org/10.1191/0959683602h519rp>.
- Jennings, A.E., Weiner, N.J., Helgadottir, G., Andrews, J.T., 2004. Modern foraminiferal faunas of the southwestern to northern Iceland shelf: oceanographic and environmental controls. *J. Foraminif. Res.* 34, 180–207. <https://doi.org/10.2113/34.3.180>.
- Jennings, A., Sheldon, C., Cronin, T., Francus, P., Stoner, J., Andrews, J., 2011. The Holocene history of Nares Strait: transition from glacial Bay to arctic-atlantic throughflow. *Oceanography* 24, 26–41. <https://doi.org/10.5670/oceanog.2011.52>.
- Jennings, A., Reilly, B., Andrews, J., Hogan, K., Walczak, M., Jakobsson, M., Stoner, J., Mix, A., Nicholls, K.W., O'Regan, M., Prins, M.A., 2022. Modern and early holocene ice shelf sediment facies from Petermann Fjord and northern Nares Strait, northwest Greenland. *Quat. Sci. Rev.* 283, 107460. <https://doi.org/10.1016/j.quascirev.2022.107460>.
- Jennings, A.E., Seidenkrantz, M.-S., Knudsen, K.L., 2020a. Glomulina oculus, new calcareous foraminiferal species from the high arctic: a potential indicator of a nearby marine-terminating glacier. *J. Foraminif. Res.* 50, 219–234. <https://doi.org/10.2113/gsjfr.52.2.219>.
- Jennings, A., Andrews, J., Reilly, B., Walczak, M., Jakobsson, M., Mix, A., Stoner, J., Nicholls, K.W., Cheseby, M., 2020b. Modern foraminiferal assemblages in northern Nares Strait, Petermann fjord, and beneath Petermann ice tongue, NW Greenland. *Arctic Antarct. Alpine Res.* 52, 491–511. <https://doi.org/10.1080/15230430.2020.1806986>.
- Johannessen, O.M., 1986. Brief overview of the physical oceanography. In: Hurdle, B.G. (Ed.), *The Nordic Seas*. Springer, New York, NY, pp. 103–128. https://doi.org/10.1007/978-1-4615-8035-5_4.
- Johnsen, S.J., Dahl-Jensen, D., Gundestrup, N., Steffensen, J.P., Clausen, H.B., Miller, H., Masson-Delmotte, V., Sveinbjörnsdóttir, A.E., White, J., 2001. Oxygen isotope and palaeotemperature records from six Greenland ice-core stations: Camp Century, Dye-3, GRIP, GISP2, Renland and NorthGRIP. *Journal of Quaternary Science: Published for the Quaternary Research Association* 16 (4), 299–307. <https://doi.org/10.1002/jqs.622>.
- Khan, S.A., Kjær, K.H., Bevis, M., Bamber, J.L., Wahr, J., Kjeldsen, K.K., Björk, A.A., Korsgaard, N.J., Stearns, L.A., van den Broeke, M.R., Liu, L., Larsen, N.K., Muresan, I.S., 2014. Sustained mass loss of the northeast Greenland ice sheet triggered by regional warming. *Nat. Clim. Change* 4, 292–299. <https://doi.org/10.1038/nclimate2161>.
- Khazendar, A., Fenty, I.G., Carroll, D., Gardner, A., Lee, C.M., Fukumori, I., Wang, O., Zhang, H., Seroussi, H., Moller, D., Noël, B.P.Y., van den Broeke, M.R., Dinardo, S., Willis, J., 2019. Interruption of two decades of Jakobshavn Isbrae acceleration and thinning as regional ocean cools. *Nat. Geosci.* 12, 277–283. <https://doi.org/10.1038/s41561-019-0329-3>.
- Kjær, K.H., Khan, S.A., Korsgaard, N.J., Wahr, J., Bamber, J.L., Hurlmann, R., van den Broeke, M., Timm, L.H., Kjeldsen, K.K., Björk, A.A., Larsen, N.K., Jørgensen, L.T., Færch-Jensen, A., Willerslev, E., 2012. Aerial photographs reveal late-20th-century dynamic ice loss in northwestern Greenland. *Science* 337, 569–573. <https://doi.org/10.1126/science.1220614>.
- Knudsen, K.L., Jiang, H., Jansen, E., Eiriksson, J., Heinemeier, J., Seidenkrantz, M.-S., 2004. Environmental changes off North Iceland during the deglaciation and the Holocene: foraminifera, diatoms and stable isotopes. *Mar. Micropaleontol.* 50, 273–305. [https://doi.org/10.1016/S0377-8398\(03\)00075-6](https://doi.org/10.1016/S0377-8398(03)00075-6).
- Koç, N., Jansen, E., Hafliðason, H., 1993. Paleoceanographic reconstructions of surface ocean conditions in the Greenland, Iceland and Norwegian seas through the last 14 ka based on diatoms. *Quat. Sci. Rev.* 12, 115–140. [https://doi.org/10.1016/0277-3791\(93\)90012-B](https://doi.org/10.1016/0277-3791(93)90012-B).
- Lambhead, P.J.D., Gooday, A.J., 1990. The impact of seasonally deposited phytodetritus on epifaunal and shallow infaunal benthic foraminiferal populations in the bathyal northeast Atlantic: the assemblage response. *Deep-Sea Res. Part A Oceanogr. Res. Pap.* 37, 1263–1283. [https://doi.org/10.1016/0198-0149\(90\)90042-T](https://doi.org/10.1016/0198-0149(90)90042-T).
- Larsen, N.K., Levy, L.B., Carlson, A.E., Buizert, C., Olsen, J., Strunk, A., Björk, A.A., Skov, D.S., 2018. Instability of the Northeast Greenland ice stream over the last 45,000 years. *Nat. Commun.* 9, 1872. <https://doi.org/10.1038/s41467-018-04312-7>.
- Larsen, N.K., Søndergaard, A.S., Levy, L.B., Olsen, J., Strunk, A., Björk, A.A., Skov, D., 2020. Contrasting modes of deglaciation between fjords and inter-fjord areas in eastern North Greenland. *Boreas* 49, 903–917. <https://doi.org/10.1111/bor.12475>.
- Laskar, J., Robutel, P., Joutel, F., Gastineau, M., Correia, A.C.M., Levrard, B., 2004. A long-term numerical solution for the insolation quantities of the Earth. *Astron. Astrophys.* 428, 261–285. <https://doi.org/10.1051/0004-6361:20041335>.
- Lloyd, J.M., 2006. Modern distribution of benthic foraminifera from Disko bugt, west Greenland. *J. Foraminif. Res.* 36, 315–331. <https://doi.org/10.2113/gsjfr.36.4.315>.
- Lloyd, J.M., Park, L.A., Kuijpers, A., Moros, M., 2005. Early Holocene palaeoceanography and deglacial chronology of Disko bugt, west Greenland. *Quat. Sci. Rev.*, Quaternary Land-ocean Correlation 24, 1741–1755. <https://doi.org/10.1016/j.quascirev.2004.07.024>.
- Lloyd, J.M., Kuijpers, A., Long, A., Moros, M., Park, L.A., 2007. Foraminiferal reconstruction of mid- to late-Holocene ocean circulation and climate variability in Disko Bugt, West Greenland. *Holocene* 17, 1079–1091. <https://doi.org/10.1177/0959683607082548>.
- Locarnini, M., Mishonov, A., Baranova, O., Boyer, T., Zweng, M., Garcia, H., Reagan, J., Seidov, D., Weathers, K., Paver, C., Smolyar, I., 2018. *World Ocean Atlas 1. Temperature*.
- Marcott, S.A., Shakun, J.D., Clark, P.U., Mix, A.C., 2013. A reconstruction of regional and global temperature for the past 11,300 years. *Science* 339, 1198–1201. <https://doi.org/10.1126/science.1228026>.
- Mayer, C., Reeh, N., Jung-Rothenhäusler, F., Huybrechts, P., Oerter, H., 2000. The subglacial cavity and implied dynamics under Nioghalvfjærdssjorden Glacier, NE-Greenland. *Geophys. Res. Lett.* 27, 2289–2292. <https://doi.org/10.1029/2000GL011514>.
- McCave, I.N., Manighetti, B., Robinson, S.G., 1995. Sortable silt and fine sediment size/composition slicing: parameters for palaeocurrent speed and palaeoceanography. *Paleoceanography* 10, 593–610. <https://doi.org/10.1029/94PA03039>.
- Moon, T., Joughin, I., Smith, B., Howat, I., 2012. 21st-Century evolution of Greenland outlet glacier velocities. *Science* 336, 576–578. <https://doi.org/10.1126/science.1219985>.
- Mouginot, J., Rignot, E., Scheuchl, B., Fenty, I., Khazendar, A., Morlighem, M., Buzzi, A., Paden, J., 2015. Fast retreat of Zachariæ Isstrøm, northeast Greenland. *Science* 350, 1357–1361. <https://doi.org/10.1126/science.1267111>.
- Mouginot, J., Rignot, E., Björk, A.A., van den Broeke, M., Millan, R., Morlighem, M., Noël, B., Scheuchl, B., Wood, M., 2019. Forty-six years of Greenland Ice Sheet mass balance from 1972 to 2018. *Proc. Natl. Acad. Sci. Unit. States Am.* 116, 9239–9244. <https://doi.org/10.1073/pnas.1904242116>.
- Mugford, R.I., Dowdeswell, J.A., 2010. Modeling iceberg-rafted sedimentation in high-latitude fjord environments. *J. Geophys. Res. Earth Surf.* 115. <https://doi.org/10.1029/2009JF001564>.
- Müller, J., Werner, K., Stein, R., Fahl, K., Moros, M., Jansen, E., 2012. Holocene cooling culminates in sea ice oscillations in Fram Strait. *Quat. Sci. Rev.* 47, 1–14. <https://doi.org/10.1016/j.quascirev.2012.04.024>.
- Nagler, T., Rott, H., Hetzinger, M., Wuite, J., Potin, P., 2015. The sentinel-1 mission: new opportunities for ice sheet observations. *Rem. Sens.* 7, 9371–9389. <https://doi.org/10.3390/rs70709371>.
- Nesje, A., Dahl, S.O., 1993. Lateglacial and Holocene glacier fluctuations and climate variations in western Norway: a review. *Quat. Sci. Rev.* 12, 255–261. [https://doi.org/10.1016/0277-3791\(93\)90081-V](https://doi.org/10.1016/0277-3791(93)90081-V).
- NGRIP-Members, 2004. High-resolution record of Northern Hemisphere climate extending into the last interglacial period. *Nature* 431, 147–151.
- Nick, F.M., Vieli, A., Howat, I.M., Joughin, I., 2009. Large-scale changes in Greenland outlet glacier dynamics triggered at the terminus. *Nat. Geosci.* 2, 110–114. <https://doi.org/10.1038/ngeo394>.
- Nørgaard-Pedersen, N., Mikkelsen, N., Kristoffersen, Y., 2008. Late glacial and Holocene marine records from the independence fjord and Wandel sea regions, north Greenland. *Polar Res.* 27, 209–221. <https://doi.org/10.1111/j.1751-8369.2008.00065.x>.
- O'Coigh, C., Dowdeswell, J.A., 2001. Laminated sediments in glaciomarine environments: diagnostic criteria for their interpretation. *Quat. Sci. Rev.* 20, 1411–1436. [https://doi.org/10.1016/S0277-3791\(00\)00177-3](https://doi.org/10.1016/S0277-3791(00)00177-3).
- Ouellet-Bernier, M.-M., de Vernal, A., Hillaire-Marcel, C., Moros, M., 2014. Paleocceanographic changes in the Disko bugt area, west Greenland, during the Holocene. *Holocene* 24, 1573–1583. <https://doi.org/10.1177/0959683614544060>.
- Pados-Dibattista, T., Pearce, C., Detlef, H., Bendtsen, J., Seidenkrantz, M.-S., 2022. Holocene palaeoceanography of the Northeast Greenland shelf. *Clim. Past* 18, 103–127. <https://doi.org/10.5194/cp-18-103-2022>.
- Perner, K., Moros, M., Lloyd, J.M., Jansen, E., Stein, R., 2015. Mid to late Holocene strengthening of the East Greenland Current linked to warm subsurface Atlantic water. *Quaternary Sci. Rev.* 129, 296–307. <https://doi.org/10.1016/j.quascirev.2015.10.007>.
- Polyak, L., Korsun, S., Febo, L.A., Stanovoy, V., Khusid, T., Hald, M., Paulsen, B.E., Lubinski, D.J., 2002. Benthic foraminiferal assemblages from the southern Kara Sea, a river-influenced Arctic marine environment. *J. Foraminif. Res.* 32, 252–273. <https://doi.org/10.2113/32.3.252>.
- Pritchard, H.D., Arthern, R.J., Vaughan, D.G., Edwards, L.A., 2009. Extensive dynamic thinning on the margins of the Greenland and Antarctic ice sheets. *Nature* 461, 971–975. <https://doi.org/10.1038/nature08471>.
- Ran, L., Jiang, H., Knudsen, K.L., Eiriksson, J., Gu, Z., 2006. Diatom response to the Holocene climatic optimum on the North Icelandic shelf. *Mar. Micropaleontol.* 60, 226–241. <https://doi.org/10.1016/j.marmicro.2006.05.002>.
- Reimer, P.J., Reimer, R.W., 2001. A marine reservoir correction database and on-line interface. *Radiocarbon* 43 (2A), 461–463.
- Reilly, B.T., Stoner, J.S., Wiest, J., 2017. Sed CT: MATLABM tools for standardized and quantitative processing of sediment core computed tomography (CT) data collected using a medical CT scanner. *Geochemistry, Geophysics, Geosystems* 18 (8), 3231–3240. <https://doi.org/10.1002/2017GC006884>.
- Reimer, P.J., Bard, E., Bayliss, A., Beck, J.W., Blackwell, P.G., Ramsey, C.B., Buck, C.E., Cheng, H., Edwards, R.L., Friedrich, M., Grootes, P.M., 2013. IntCal13 and Marine13 radiocarbon age calibration curves 0–50,000 years cal BP. *Radiocarbon*

- 55 (4), 1869–1887.
- Richter, T.O., van der Gaast, S., Koster, B., Vaars, A., Gieles, R., Stigter, H.C. de, Haas, H.D., van Weering, T.C.E. van, 2006. The Aavaect XRF Core Scanner: technical description and applications to NE Atlantic sediments. *Geol. Soc. Lond. Spec. Publ.* 267, 39–50. <https://doi.org/10.1144/GSL.SP.2006.267.01.03>.
- Rignot, E., Mouginot, J., 2012. Ice flow in Greenland for the international polar year 2008–2009. *Geophys. Res. Lett.* 39. <https://doi.org/10.1029/2012GL051634>.
- Rignot, E., Box, J.E., Burgess, E., Hanna, E., 2008. Mass balance of the Greenland ice sheet from 1958 to 2007. *Geophys. Res. Lett.* 35. <https://doi.org/10.1029/2008GL035417>.
- Risebrobakken, B., Dokken, T., Smedsrud, L.H., Andersson, C., Jansen, E., Moros, M., Ivanova, E.V., 2011. Early Holocene temperature variability in the Nordic Seas: the role of oceanic heat advection versus changes in orbital forcing. *Paleoceanography* 26. <https://doi.org/10.1029/2011PA002117>.
- Rudels, B., Jones, E.P., Anderson, L.G., Kattner, G., 1994. On the intermediate depth waters of the Arctic Ocean. In: *The Polar Oceans and Their Role in Shaping the Global Environment*. American Geophysical Union (AGU), pp. 33–46. <https://doi.org/10.1029/GM085p0033>.
- Rudels, B., Björk, G., Nilsson, J., Winsor, P., Lake, I., Nohr, C., 2005. The interaction between waters from the Arctic Ocean and the nordic seas north of Fram Strait and along the east Greenland current: results from the Arctic Ocean-02 ocean expedition. *J. Mar. Syst.* 55, 1–30. <https://doi.org/10.1016/j.jmarsys.2004.06.008>.
- Rudels, B., Korhonen, M., Budéus, G., Beszczynska-Möller, A., Schauer, U., Nummelin, A., Quadfasel, D., Valdimarsson, H., 2012. The East Greenland Current and its impacts on the Nordic Seas: observed trends in the past decade. *ICES J. Mar. Sci.* 69, 841–851. <https://doi.org/10.1093/icesjms/fss079>.
- Rueden, C.T., Schindelin, J., Hiner, M.C., DeZonia, B.E., Walter, A.E., Arena, E.T., Eliceiri, K.W., 2017. ImageJ2: ImageJ for the next generation of scientific image data. *BMC Bioinf.* 18, 529. <https://doi.org/10.1186/s12859-017-1934-z>.
- Ruff, M., Szidat, S., Gäggeler, H.W., Suter, M., Synal, H.-A., Wacker, L., 2010. Gaseous radiocarbon measurements of small samples. *Nucl. Instrum. Methods Phys. Res. Sect. B Beam Interact. Mater. At., Proceedings of the Eleventh International Conference on Accelerator Mass Spectrometry* 268, 790–794. <https://doi.org/10.1016/j.nimb.2009.10.032>.
- Schaffer, J., Appen, W.-J. von, Dodd, P.A., Hofstede, C., Mayer, C., Steur, L. de, Kanzow, T., 2017. Warm water pathways toward Nioghalvfjærdssjorden Glacier, northeast Greenland. *J. Geophys. Res. Oceans* 122, 4004–4020. <https://doi.org/10.1002/2016JC012462>.
- Schaffer, J., Kanzow, T., von Appen, W.-J., von Albedyll, L., Arndt, J.E., Roberts, D.H., 2020. Bathymetry constrains ocean heat supply to Greenland's largest glacier tongue. *Nat. Geosci.* 13, 227–231. <https://doi.org/10.1038/s41561-019-0529-x>.
- Seale, A., Christoffersen, P., Mugford, R.I., O'Leary, M., 2011. Ocean forcing of the Greenland Ice Sheet: calving fronts and patterns of retreat identified by automatic satellite monitoring of eastern outlet glaciers. *J. Geophys. Res. Earth Surf.* 116. <https://doi.org/10.1029/2010JF001847>.
- Seidenkrantz, M.-S., 1995. *Cassidulina teretis* Tappan and *Cassidulina neoteretis* new species (Foraminifera): stratigraphic markers for deep sea and outer shelf areas. *J. Micropaleontol.* 14, 145–157. <https://doi.org/10.1144/jm.14.2.145>.
- Seidenkrantz, M.-S., 2013. Benthic foraminifera as palaeo sea-ice indicators in the subarctic realm – examples from the Labrador Sea–Baffin Bay region. *Quat. Sci. Rev.* Sea Ice in the Paleoclimate System: the Challenge of Reconstructing Sea Ice from Proxies 79, 135–144. <https://doi.org/10.1016/j.quascirev.2013.03.014>.
- Seidenkrantz, M.-S., Andersen, J.R., Andresen, K.J., Bendtsen, J., Brice, C., Ellegaard, M., Eriksen, L.N., Gariboldi, K., Le Duc, C., Mathiasen, A.M., Nielsen, T., Ofstad, S., Pearce, C., Rasmussen, T.L., Ribeiro, S., Rysgaard, S., Røy, H., Scholze, C., Schultz, M., Wangner, D.J., 2018. NorthGreen2017 – a marine research expedition to NE Greenland onboard 'R/V Dana. Cruise Report.
- Shepherd, A., Ivins, E., Rignot, E., Smith, B., van den Broeke, M., Velicogna, I., Whitehouse, P., Briggs, K., Joughin, I., Krinner, G., Nowicki, S., Payne, T., Scambos, T., Schlegel, N., G. A., Agosta, C., Ahlström, A., Babonis, G., Barletta, V.R., Björk, A.A., Blazquez, A., Bonin, J., Colgan, W., Csatho, B., Cullather, R., Engdahl, M.E., Felikson, D., Fettweis, X., Forsberg, R., Hogg, A.E., Gallee, H., Gardner, A., Gilbert, L., Gourmelen, N., Groh, A., Gunter, B., Hanna, E., Harig, C., Helm, V., Horvath, A., Horwath, M., Khan, S., Kjeldsen, K.K., Konrad, H., Langen, P.L., Lecavalier, B., Loomis, B., Luthcke, S., McMillan, M., Melini, D., Mernild, S., Mohajerani, Y., Moore, P., Mottram, R., Mouginot, J., Moyano, G., Muir, A., Nagler, T., Nield, G., Nilsson, J., Noël, B., Otsuka, I., Pattle, M.E., Peltier, W.R., Pie, N., Rietbroek, R., Rott, H., Sandberg Sørensen, L., Sasgen, I., Save, H., Scheuchl, B., Schrama, E., Schröder, L., Seo, K.-W., Simonsen, S.B., Slater, T., Spada, G., Sutterley, T., Talpe, M., Tarasov, L., van de Berg, W.J., van der Wal, W., van Wessem, M., Vishwakarma, B.D., Wiese, D., Wilton, D., Wagner, T., Wouters, B., Wuite, J., 2020. Mass balance of the Greenland ice sheet from 1992 to 2018. *Nature* 579, 233–239.
- Ślubowska-Woldengen, M., Rasmussen, T.L., Koç, N., Klitgaard-Kristensen, D., Nilsen, F., Solheim, A., 2007. Advection of atlantic water to the western and northern svalbard shelf since 17,500calyr BP. *Quat. Sci. Rev.* 26, 463–478. <https://doi.org/10.1016/j.quascirev.2006.09.009>.
- Stein, R., 2008. *Arctic Ocean Sediments: Processes, Proxies, and Paleoenvironment*. Elsevier.
- Stein, R., Dittmers, K., Fahl, K., Kraus, M., Matthiessen, J., Niessen, F., Pirrung, M., Polyakova, Y., Schoster, F., Steinke, T., Fütterer, D.K., 2004. Arctic (palaeo) river discharge and environmental change: evidence from the Holocene Kara Sea sedimentary record. *Quat. Sci. Rev., Quaternary Environments of the Eurasian North (QUEEN)* 23, 1485–1511. <https://doi.org/10.1016/j.quascirev.2003.12.004>.
- Straneo, F., Sutherland, D.A., Holland, D., Gladish, C., Hamilton, G.S., Johnson, H.L., Rignot, E., Xu, Y., Koppes, M., 2012. Characteristics of ocean waters reaching Greenland's glaciers. *Ann. Glaciol.* 53, 202–210. <https://doi.org/10.3189/2012AoG60A059>.
- Stroeve, J.C., Kattsov, V., Barrett, A., Serreze, M., Pavlova, T., Holland, M., Meier, W.N., 2012. Trends in Arctic sea ice extent from CMIP5, CMIP3 and observations. *Geophys. Res. Lett.* 39. <https://doi.org/10.1029/2012GL052676>.
- Strunk, A., Larsen, N.K., Nilsson, A., Seidenkrantz, M.-S., Levy, L.B., Olsen, J., Lauridsen, T.L., 2018. Relative sea-level changes and ice sheet history in find-erup land, north Greenland. *Front. Earth Sci.* 6. <https://doi.org/10.3389/feart.2018.00129>.
- Syring, N., Lloyd, J.M., Stein, R., Fahl, K., Roberts, D.H., Callard, L., O'Coiffaigh, C., 2020a. Holocene interactions between glacier retreat, sea ice formation, and atlantic water advection at the inner Northeast Greenland continental shelf. *Paleoceanogr. Paleoclimatol.* 35, e2020PA004019. <https://doi.org/10.1029/2020PA004019>.
- Syring, N., Stein, R., Fahl, K., Vahlenkamp, M., Zehlich, M., Spielhagen, R.F., Niessen, F., 2020b. Holocene changes in sea-ice cover and polynya formation along the eastern North Greenland shelf: new insights from biomarker records. *Quat. Sci. Rev.* 231, 106173. <https://doi.org/10.1016/j.quascirev.2020.106173>.
- Tabone, I., Robinson, A., Alvarez-Solas, J., Montoya, M., 2019. Submarine melt as a potential trigger of the north east Greenland ice stream margin retreat during marine isotope stage 3. *Cryosphere* 13, 1911–1923. <https://doi.org/10.5194/tc-13-1911-2019>.
- Thomas, R., Frederick, E., Krabill, W., Manizade, S., Martin, C., 2009. Recent changes on Greenland outlet glaciers. *J. Glaciol.* 55, 147–162. <https://doi.org/10.3189/002214309788608958>.
- van den Broeke, M.R., Enderlin, E.M., Howat, I.M., Kuipers Munneke, P., Noël, B.P.Y., van de Berg, W.J., van Meijgaard, E., Wouters, B., 2016. On the recent contribution of the Greenland ice sheet to sea level change. *Cryosphere* 10, 1933–1946. <https://doi.org/10.5194/tc-10-1933-2016>.
- Vilks, G., 1969. Recent foraminifera in the canadian arctic. *Micropaleontology* 15, 35–60.
- Vilks, G., 1989. Ecology of recent foraminifera on the Canadian continental shelf of the Arctic Ocean. In: Herman, Y. (Ed.), *The Arctic Seas: Climatology, Oceanography, Geology, and Biology*. Springer US, Boston, MA, pp. 497–569. https://doi.org/10.1007/978-1-4613-0677-1_21.
- Vinther, B.M., Buchardt, S.L., Clausen, H.B., Dahl-Jensen, D., Johnsen, S.J., Fisher, D.A., Koerner, R.M., Raynaud, D., Lipenkov, V., Andersen, K.K., Blunier, T., 2009. Holocene thinning of the Greenland ice sheet. *Nature* 461 (7262), 385–388. <https://doi.org/10.1038/nature08355>.
- Wacker, L., Fahrni, S.M., Hajdas, I., Molnar, M., Synal, H.-A., Szidat, S., Zhang, Y.L., 2013a. A versatile gas interface for routine radiocarbon analysis with a gas ion source. *Nucl. Instrum. Methods Phys. Res. Sect. B Beam Interact. Mater. At. In: Proceedings of the Twelfth International Conference on Accelerator Mass Spectrometry*, pp. 315–319. <https://doi.org/10.1016/j.nimb.2012.02.009>. Wellington, New Zealand, 20–25 March 2011 294.
- Wacker, L., Lippold, J., Molnar, M., Schulz, H., 2013b. Towards radiocarbon dating of single foraminifera with a gas ion source. *Nucl. Instrum. Methods Phys. Res. Sect. B Beam Interact. Mater. At. In: Proceedings of the Twelfth International Conference on Accelerator Mass Spectrometry*, pp. 307–310. <https://doi.org/10.1016/j.nimb.2012.08.038>. Wellington, New Zealand, 20–25 March 2011 294.
- Wanick, J.J., Schulz-Bull, D.E., Kuss, J., Blanz, T., 2005. Long time series of deep water particle flux in three biogeochemical provinces of the northeast Atlantic. *J. Mar. Syst.* 56, 391–415. <https://doi.org/10.1016/j.jmarsys.2005.03.001>.
- Weatherall, P., Marks, K.M., Jakobsson, M., Schmitt, T., Tani, S., Arndt, J.E., Rovere, M., Chayes, D., Ferrini, V., Wigley, R., 2015. A new digital bathymetric model of the world's oceans. *Earth Space Sci.* 2, 331–345. <https://doi.org/10.1002/2015EA000107>.
- Werner, K., Müller, J., Husum, K., Spielhagen, R.F., Kandiano, E.S., Polyak, L., 2016. Holocene sea subsurface and surface water masses in the Fram Strait – comparisons of temperature and sea-ice reconstructions. *Quat. Sci. Rev., Special Issue: PAST Gateways (Palaeo-Arctic Spatial and Temporal Gateways)* 147, 194–209. <https://doi.org/10.1016/j.quascirev.2015.09.007>.
- Williams, K.M., Andrews, J.T., Weiner, N.J., Mudie, P.J., 1995. Late quaternary paleoceanography of the mid- to outer continental shelf, east Greenland. *Arct. Alp. Res.* 27, 352–363. <https://doi.org/10.1080/00040851.1995.12003132>.
- Wilson, N.J., Straneo, F., 2015. Water exchange between the continental shelf and the cavity beneath Nioghalvfjærdssjøen (79 North Glacier). *Geophys. Res. Lett.* 42, 7648–7654. <https://doi.org/10.1002/2015GL064944>.

- Winkelmann, D., Jokat, W., Jensen, L., Schenke, H.-W., 2010. Submarine end moraines on the continental shelf off NE Greenland – implications for Lateglacial dynamics. *Quat. Sci. Rev.* 29, 1069–1077. <https://doi.org/10.1016/j.quascirev.2010.02.002>.
- Wollenburg, J.E., Mackensen, A., 1998. Living benthic foraminifers from the central Arctic Ocean: faunal composition, standing stock and diversity. *Mar. Micro-paleontol.* 34, 153–185. [https://doi.org/10.1016/S0377-8398\(98\)00007-3](https://doi.org/10.1016/S0377-8398(98)00007-3).
- Wollenburg, J.E., Knies, J., Mackensen, A., 2004. High-resolution paleoproductivity fluctuations during the past 24 kyr as indicated by benthic foraminifera in the marginal Arctic Ocean. *Palaeogeogr. Palaeoclimatol. Palaeoecol.* 204, 209–238. [https://doi.org/10.1016/S0031-0182\(03\)00726-0](https://doi.org/10.1016/S0031-0182(03)00726-0).
- Wood, M., Rignot, E., Fenty, I., An, L., Bjørk, A., van den Broeke, M., Cai, C., Kane, E., Menemenlis, D., Millan, R., Morlighem, M., Mouginot, J., Noël, B., Scheuchl, B., Velicogna, I., Willis, J.K., Zhang, H., 2021. Ocean forcing drives glacier retreat in Greenland. *Sci. Adv.* 7, eaba7282. <https://doi.org/10.1126/sciadv.aba7282>.
- Yang, J., Luo, Z., Tu, L., 2020. Ocean access to Zachariæ Isstrøm glacier, northeast Greenland, revealed by OMG airborne gravity. *J. Geophys. Res. Solid Earth* 125, e2020JB020281. <https://doi.org/10.1029/2020JB020281>.
- Zehnich, M., Spielhagen, R.F., Bauch, H.A., Forwick, M., Hass, H.C., Palme, T., Stein, R., Syring, N., 2020. Environmental variability off NE Greenland (western Fram Strait) during the past 10,600 years. *Holocene* 30, 1752–1766. <https://doi.org/10.1177/0959683620950393>.